Utah State University
DigitalCommons@USU

All Graduate Plan B and other Reports | Graduate Studies

5-2012

# In Situ Method of Measuring Atmosphere Neutral Winds with a Rigid Falling Sphere

Joshua F. Martineau
*Utah State University*

Follow this and additional works at: https://digitalcommons.usu.edu/gradreports

 Part of the Mechanical Engineering Commons

## Recommended Citation

Martineau, Joshua F., "In Situ Method of Measuring Atmosphere Neutral Winds with a Rigid Falling Sphere" (2012). *All Graduate Plan B and other Reports*. 183.
https://digitalcommons.usu.edu/gradreports/183

This Report is brought to you for free and open access by the Graduate Studies at DigitalCommons@USU. It has been accepted for inclusion in All Graduate Plan B and other Reports by an authorized administrator of DigitalCommons@USU. For more information, please contact digitalcommons@usu.edu.

# IN SITU METHOD OF MEASURING ATMOSPHERE NEUTRAL WINDS WITH A RIGID FALLING SPHERE

by

Joshua F. Martineau

A report submitted in partial fulfillment
Of the requirements of the degree

of

MASTER OF SCIENCE

in

Mechanical Engineering

Approved:

_____
Dr. Stephen A. Whitmore
Major Professor

_____
Dr. R. Rees Fullmer
Committee Member

_____
Dr. David Geller
Committee Member

UTAH STATE UNIVERSITY

Logan, Utah

2012

# ABSTRACT

In Situ Method of Measuring Atmosphere Neutral

Winds with a Rigid Falling Sphere

by

Joshua F. Martineau, Master of Science

Utah State University, 2012

Major Professor: Dr. Stephen A. Whitmore

Department: Mechanical and Aerospace Engineering

The new falling sphere instruments will measure lower E-region winds and density, which are critical for many of the electrodynamics and plasma physics studies that are carried out as part of the NASA suborbital rocket program. The new falling sphere design will take advantage of modern commercially available electronic components and materials. Of primary importance, it is proposed to fly an *in-situ* instrument that targets the measurement of neutral wind profiles over the altitude range from 80 to 150 km, with accuracy better than that achieved in previous implementations of the falling sphere technique and those typically obtained with the chemical release technique. The falling sphere instrument will measure the lower E-region winds and density, which are critical for many of the electrodynamics and plasma physics studies that are carried out as part of the NASA Geospace suborbital rocket program. This gives a report of the overall design and the rigid body dynamics involved as well as some post flight analysis.

(91 pages)

## ACKNOWLEDFMENTS

I would like to thank Chad Fish for his continual push and encouragement through the life of this monster of a project, and for the many others at SDL who gave their time and talents to making this completion a success.

I would like to thank my committee members, Drs. Stephen A. Whitmore, David Geller, and R. Rees Fullmer for their support and guidance throughout the life of this project and the inspiration they give.

# CONTENTS

# LIST OF TABLES

Page

# LIST OF FIGURES

Page

# LIST OF ACRONYMS

$cg$ = center of gravity

$CM$ = Center of Mass

$Co-I$ = Co-Investigator

$DCM$ = Direct Cosine Matrix

$ECF$ = Earth Centered Fixed coordinate reference frame

$ECI$ = Earth Centered Inertial coordinate reference frame

$FSP$ = Falling Sphere Probe (aka, sphere)

$GPS$ = Global Positioning System

$IMU$ = Inertial Measurement Unit

$MOI$ = Moment of Inertia

$NOVA$ = Nanosat Operation Verification & Assessment (Test Facility)

$NSF$ = National Science Foundation

$NSROC$ = NASA Rocket Operations Contract

$PCM$ = Pulse-code Modulation

$PI$ = Principle Investigator

$PDOP$ = Position Dilution of Precision

$POI$ = Product of Inertia

$SCF$ = Sphere Centered Fixed coordinate reference frame

$SDL$ = Space Dynamics Laboratory

$USU$ = Utah State University

$UTC$ = Coordinated Universal Time

$WFF$ = Wallop's Flight Facility

# NOMENCLATURE

| | |
|---|---|
| A | = reaction point 1 of CM table |
| $A$ | = generic rotation matrix, DCM |
| $A_{ref}$ | = reference area |
| $Az$ | = azimuth angle |
| $A_{ch}$ | = vector containing all accelerometer channel measurements |
| $a$ | = semi-major axis of Earth |
| $a_{BF}$ | = translational acceleration due to external body forces |
| $a_{chan*}$ | = acceleration measured on channel * |
| $a_D$ | = acceleration due to drag |
| $a_I$ | = acceleration in the Inertial frame |
| $a_c$ | = centripetal acceleration |
| B | = reaction point 2 of CM table |
| C | = reaction point 3 of CM table |
| $\boldsymbol{C}$ | = matrix of coefficients defined in Eq. (4.7.5) |
| $C_D$ | = drag coefficient |
| $C_{D;Total}$ | = total drag coefficient |
| $C_{D;P}$ | = pressure drag coefficient |
| $C_{D;f}$ | = skin friction drag coefficient |
| $C_{D;SW}$ | = shockwave drag coefficient |
| $C_{D;EX}$ | = drag coefficient due to excrescencies |
| $C_L$ | = lift coefficient |
| D | = width between load cells 2 & 3 of CM table |
| $ECF$ | = x component of position in ECF coordinates |
| $El$ | = elevation angle |
| $e$ | = eccentricity of Earth |

$F_{body}$ = body force per unit volume

$F_{BF}$ = total external body forces

$F_D$ = force due to drag

$F_{D;P}$ = drag force due to pressure drag

$F_g$ = gravitational force

$F_L$ = force due to lift

$F_M$ = Magnus force

$f$ = frequency

$G$ = gravitational constant

$\boldsymbol{G}$ = white noise coefficient in the dynamics model

$g$ = acceleration due to gravity

$H$ = sensitivity matrix

$H_G$ = angular momentum vector

$h$ = altitude

$h$ = estimated measurement output

$h_{Terrier}$ = altitude of launch vehicle at time of ejection of sphere

$h_{vert}$ = vertical offset from CG to the vertically mounted accelerometer

$K$ = Kalman gain

$L$ = perpendicular distance from load cell 1 to load cells 2 & 3 of CM table

$I$ = inertia

$I_{calibrate}$ = inertia of calibration item about the rotation axis (i.e. steel ball bearing)

$I_O$ = inertia of oscillating system about the rotation axis

$I_{object}$ = inertia of the object of interest about the rotation axis

$I_T$ = total inertia of combined objects about the rotation axis

$I_{A**}$ = measured oscillation to calculate POI about the rotation axis for **, defined in Eq. (6.2.12)

$I_{table}$ = inertia of MOI table about the rotation axis

$I_{total;setup}$ = combined inertias of all items except the object of interest about the rotation axis

$\hat{\imath}_*$ = unit vector in the direction of *

$\hat{\imath}_D$ = unit vector in the direction of "Down" of the NED reference frame

$\hat{\imath}_E$ = unit vector in the direction of "East" of the NED reference frame

$\hat{\imath}_{FM}$ = unit vector in the direction of the Magnus force, defined in Eq. (4.5.4)

$\hat{\imath}_{H_G}$ = unit vector in the direction of the angular momentum vector

$\hat{\imath}_N$ = unit vector in the direction of "North" of the NED reference frame

$\hat{\imath}_{V_{FSP}}$ = unit vector in the direction of the velocity of the Falling Sphere Probe

$\hat{\imath}_{V_\perp}$ = unit vector in the direction of the perpendicular velocity

$\hat{\imath}_{\omega_{FSP}}$ = unit vector in the direction of the axis of rotation of the Falling Sphere Probe

$\boldsymbol{J}$ = inertia matrix

$k_O$ = oscillation spring constant

$k_{table}$ = MOI table stiffness constant

$L$ = perpendicular distance from load cell 1 to load cells 2 & 3 of CM table

$M$ = Earth's mass

$M_x$ = moment about the x-axis

$M_y$ = moment about the y-axis

$m$ = mass

$m_{FSP}$ = Falling Sphere Probe mass

$N$ = length of the normal to an ellipsoid

$P$ = pressure

$\boldsymbol{P}$ = error-covariance matrix

$\boldsymbol{P}_{gyro}$ = error-covariance matrix for the gyro sensor

$\boldsymbol{P}_{attitude}$ = error-covariance matrix for the attitude orientation

$P_{**}$ = product of inertia for position **

$Q$ = process noise covariance, defined in Table 4 for discrete systems

$q$ = quaternion

$q_I^B$ = inertial to body quaternion

$\dot{q}$ = time derivative of the quaternion

$R$ = measurement-error covariance

$R_{sc}$ = position from center of earth to spacecraft cg

$R_{By}$ = vector in the direction of the spin axis of the sphere

$Re$ = Reynolds number

$\boldsymbol{R}_I^B$ = inertial to body rotation matrix

$\boldsymbol{R}_{ECI}^B$ = ECI to body rotation matrix

$\boldsymbol{R}_{ECI}^{NED}$ = ECI to NED rotation matrix

$\boldsymbol{R}_{NED}^B$ = NED to body rotation matrix

$R_{Terrier}$ = range of launch vehicle at time of ejection of sphere

$r$ = radius

$\vec{r}$ = arbitrary position vector between two masses

$\ddot{\vec{r}}$ = arbitrary acceleration vector

$r_{angled}$ = radial offset from CG to the angle mounted accelerometer

$r_{FSP}$ = radius of the Falling Sphere Probe

$r_{horz}$ = horizontal offset from CG to the angle mounted accelerometer

$r_{vert}$ = vertical offset from CG to the angle mounted accelerometer

$T$ = external torques

$\boldsymbol{T}_B$ = body torques

$\boldsymbol{T}_{F_{D;f}}$ = torque caused by the drag force due to skin friction

$T_O$ = period of oscillation

$T_{calibrate}$ = period of oscillation of calibration setup

$T_{table}$ = period of oscillation of MOI table only

$T_{total}$ = period of oscillation for entire system, including table, fixtures, frames, and object of interest

$t$ = time

$t_{eject}$ = time of ejection

$UP$ = negative “down” vector in NED coordinates (“up” vector in NEU coordinates)

$\hat{\boldsymbol{u}}_*$ = unit vector in the direction of *

$V$ = velocity

$V_\perp$ = velocity perpendicular to the axis of rotation

$V_\infty$ = freestream velocity

W = total weight

$X$ = state variable vector

$x$ = x-axis location of the center of mass on the CM table

$x_{cm}$ = center of mass

$x_{cp}$ = distance to center of pressure

$X_{ECF}$ = x component of position in ECF coordinates

$y$ = y-axis location of the center of mass on the CM table

$Y_{ECF}$ = y component of position in ECF coordinates

$Z_{ECF}$ = z component of position in ECF coordinates

$\beta$ = bias of the gyro

$\delta\alpha$ = attitude small angle approximation

$\delta\beta$ = gyro small rate approximation

$\Delta\beta$ = error-bias estimation

$\Delta t$ = sampling interval in the gyro

$\Delta x$ = error-state estimation

$\epsilon$ = measurement residual

$\theta_n$ = nutation angle

$\vartheta$ = orientation angle for measuring oscillation to calculate POIs

$\lambda$ = east longitude

$\mu$ = gravitational parameter defined in Eq. (4.1.12)

$\nu$ = input white noise in dynamics model

$\Xi$ = quaternion dynamics update coefficient, defined in Table 4

$\rho$ = density

$\rho_\infty$ = freestream density

$\varrho$ = vector part of the quaternion

$\sigma_g$ = standard deviation of the gyro

$\tau$ = oscillation time constant

$\Phi$ = state transition matrix, define in Table 4 for discrete systems

$\varphi$ = oscillation angle of rotation

$\phi$ = latitude

$\widehat{\boldsymbol{\psi}}$ = quaternion dynamics propagate coefficient, defined in Table 4

$\boldsymbol{\Omega}$ = constant defined in Eq. (4.1.5)

$\bar{\boldsymbol{\Omega}}$ = quaternion dynamics propagate coefficient, defined in Table 4

$\omega$ = angular velocity

$\omega_B$ = angular velocity in body coordinates

$\omega_E$ = angular velocity of the earth

$\omega_p$ = precession rate

$\omega_s$ = spin rate about axis of symmetry

$\dot{\omega}$ = angular acceleration

**Superscripts**

$T$ = transpose

$+$ = Kalman Filter update state

$-$ = Kalman Filter propagated state

**Subscripts**

0 = initial conditions

$k$ = current time step

$x$ = associated with the x-component or axis

$y$ = associated with the y-component or axis

$z$ = associated with the z-component or axis

**Other notation**

$\hat{}$ = (hat) unit vector

$\hat{}$ = (hat) Kalman Filter estimation

$\tilde{}$ = (tilde) measurement output

bold = denotes a matrix

$[\cdot\times]$ = cross product matrix for $(\cdot)$

$\nabla$ = differential operator, del

# INTRODUCTION

OVER the past five decades, nearly all *in-situ* E-region wind profile measurements have been made with the chemical release technique. In the 1960's, a large number of chemical release measurements were made at various sites around the world to establish a climatology of the winds and wind fluctuations. More recently, such wind measurements have become a more-or-less standard part of NASA sounding rocket campaigns/experiments that focus on electrodynamics, plasma physics, or neutral dynamics of the E-region/lower thermosphere. For example, in the Coqui 2 campaign in Puerto Rico in 1998, three of the five experiments that constituted the campaign included chemical release wind measurements[1]. In the more recent EQUIS 2 campaign in Kwajalein, three of the four experiments that constituted the campaign included chemical release wind measurements[2]. *Larsen* (2002) has summarized the chemical release wind measurements made since the first experiment in 1957, including the characteristics of the measured winds. To date, more than 500 such wind profile measurements have been made.

The chemical release wind measurement technique involves the release of a chemical tracer in the upper atmosphere that is visible from the ground and that can be tracked optically. A large variety of chemicals have been used over the years, including some that become ionized and serve as tracers of the plasma motion (e.g., barium), and others that serve as tracers of the neutral motion. The primary neutral tracer chemicals have been sodium, lithium, and TMA. In general, the chemical release technique has been very successful, yielding wind profile measurements over a large fraction of the E-region altitude range with good height resolution (250-500 meters) and small error bars (3-10 m/s). TMA measurements have been shown to be in good agreement with lidar wind measurements made in the same altitude range as the TMA in the mesosphere and lower thermosphere (MLT) region where the two measurements overlap[3].

There are drawbacks to the chemical release technique, however. For example, both sodium and lithium require solar illumination to be visible from the ground and therefore are used solely for twilight releases when the trails are in sunlight and the ground station is in darkness. Lithium has been used to a much more limited extent for daytime wind measurements by observing the releases with cameras equipped with special narrow filters. The requirement for solar illumination significantly limits the application of those chemicals in experiments that focus on specific geophysical phenomena. TMA, on the other hand, is

chemiluminescent and can be deployed at any time during the night, making it more versatile. The latter chemical has therefore been used in the vast majority of the E-region chemical release wind measurements. A further drawback is related to the operational aspects of sounding rocket experiments that include chemical release measurements in that the combination of the clear-sky requirements and the geophysical condition requirements generally extends the launch window beyond what it would be if the geophysical conditions alone dictated the launch conditions. NASA maintains sky condition requirements for their launches as dictated by safety concerns, but they only apply to the launch site and can accommodate much more cloud cover than the chemical release technique permits.

*In-situ* instrument measurements of the neutral winds would therefore provide significant advantages for the typical sounding rocket campaign/experiment since measurements would be possible over a much broader range of solar illumination conditions and the restrictive clear-sky requirement would be almost entirely eliminated. Only a few *in-situ* instrument measurements of the E-region neutral winds have been attempted, primarily because any measurements that require sampling of the atmosphere on the rocket platform are difficult to implement due to interaction of the rocket body with the target medium. A notable exception is the falling sphere measurements made by R. Philbrick and co-workers in the 1970's and 1980's [4]. Only a relatively small number of falling sphere measurements were made in the past but the results from those measurements suggest that the technique is a viable alternative to the chemical release technique, with height resolution, altitude coverage, and error bars comparable to the release technique. The technical challenges associated with the falling sphere measurement are primarily related to the high-sensitivity required of the instrument accelerometers, which are the key sensors for the technique, and the tracking and attitude determination of the sphere. Recent improvements in high-resolution ultra-sensitive commercial accelerometers, as well as the availability of miniature GPS tracking systems and inertial measurement unit attitude determination systems, make it possible to develop a new high-performance falling sphere instrument for wind measurement applications that is not limited by operational restrictions of the chemical release technique. Ultimately, the development of this new falling sphere instrument will enable the deployment of multiple falling spheres from one rocket for 3D determination of neutral wind measurements.

## PREVIOUS HISTORY

The Active Falling Sphere (AFS), as it was termed, was developed in the 1970s as an *in-situ* sounding rocket instrument for measuring neutral density and wind velocity, turbulence, and wave structure [4], [5]throughout the D- and E-regions. The AFS was used on ten successful flights between the late-1970s and mid-1980s [6]. The AFS achieved accuracy (sensitivity) levels of approximately 2-5 m/s for wind velocity measurements and 10-9 kg/m$^3$ for density measurements, with a vertical resolution of approx. 100 m.

A fairly massive 25 cm sphere was cradled in the rocket payload section. Following nose cone ejection, the sphere was ejected at a typical altitude of 65 km on the upleg at a velocity of approximately 4 m/s from a spring-loaded cradle. The cradle was designed to minimize torque during the ejection of the sphere and limit the precession cone angle of the sphere spin axis (z-axis). The sphere was often released with a z-axis spin of approximately 6 Hz. The z-axis moment of inertia was adjusted using a rotating pendulum to be approximately 15% greater than the uniform moment of inertia of any axis in the orthogonal plane. This resulted in a precession frequency of approximately 1 Hz [5].

The AFS sphere contained a sensitive 3-axis piezoelectric accelerometer, a less sensitive single-axis accelerometer, a telemetry encoder and transmitter, transponder, and other supporting structure and electronics. The 3-axis accelerometer was used for wind and density measurements. The single-axis accelerometer was used to monitor the magnitude of the precession cone angle and precession acceleration. The transponder was used for accurate trajectory tracking as an altitude trajectory error of 60 m results in an apparent 1% density error.

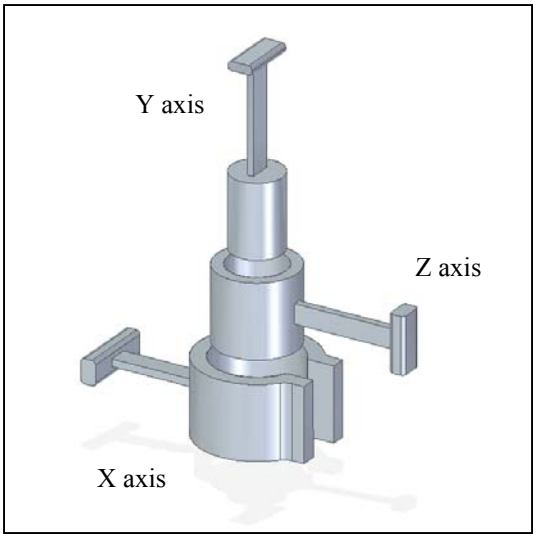


**Figure 1. Schematic of the AFS 3-axis accelerometer configuration (Philbrick et al., 1978)**

Figure 1 shows the 3-axis accelerometer configuration that was designed and made specifically for use in those early experiments. Three separate tungsten proof masses were suspended by piezoelectric crystal bimorph arms which were then secured to an enclosure fabricated from a solid block of metal. Caging jaws were used to secure the proof masses until the sphere was ejected from the rocket payload section. This prevented fracture of the bimorph arms during handling and launch operations. The system was calibrated using a forced simple harmonic oscillator. This design resulted in measurement sensitivity of ~ 10-8 $m/s^2$ (10-9 g).

## PURPOSE

Our proposal objective is to develop and carry out an in-flight test and calibration of a next-generation falling sphere instrument for E-region neutral wind and density profile measurements. This new falling sphere instrument will measure lower E-region winds and density, which are critical for many of the electrodynamics and plasma physics studies that are carried out as part of the NASA suborbital rocket program. Temperature profiles can also be derived from the density profile by using the hydrostatic equation. The new falling sphere design will take advantage of modern commercially available electronic components and materials. Of primary importance, we propose to develop an *in-situ* instrument that targets the measurement of neutral wind profiles over the altitude range from 90 to 150 km, with accuracy better than that achieved in previous implementations of the falling sphere technique and those typically obtained with the chemical release technique. In addition, the proposed measurement technique will not be subject to stringent ground weather and solar illumination conditions.

# DYNAMICS

In flight dynamics there are three types of forces acting on the vehicle: propulsion forces, gravitational forces, and aerodynamic forces [7]. In this case, the FSP has no propulsive forces, and the dynamics are described only from the gravitational and aerodynamic forces.

A 6-DOF approach decomposes the rigid-body motion into a translation of the center of mass and a rotation about an axis passing through the center of mass location. The position of the center of mass is updated using Newton's laws of motion in the inertial frame, while the rotation of the body is determined by numerically integrating Euler's equations of motion in a body principal-axis system. The rotational position of the body is specified using Euler parameters, which are updated by numerical integration of the angular velocity.

## A. Governing Equations

In order to understand the motion of an object moving through a fluid, air in this case, an understanding of the forces and moments acting on the object must be known. Through Newton's second law, i.e. F = ma, and under the assumption of inviscid flow, the forces and moments are calculated. These forces and moments are the aerodynamic forces and moments and gravitational forces. The aerodynamic forces of interest are the forces due to drag and lift, expressed as,

$$F_D = \frac{1}{2}\rho_\infty V_\infty^2 A_{ref} C_D \tag{4.1.1}$$

$$F_L = \frac{1}{2}\rho_\infty V_\infty^2 A_{ref} C_L \tag{4.1.2}$$

The equations of motion for a rigid body undergoing both translation and rotation with respect to some inertial frame are also derived from Newton's second law. From the total angular momentum, *Euler's equations of motion are* derived. This derivation is shown in detail in ref[8]. This, in conjunction with the kinematic equation, fully describes the rotational motion of a rigid vehicle. The use of a quaternion method is preferred. The Euler and kinematic equations are, respectively,

$$\boldsymbol{J}\dot{\omega} = -[\omega \times]\boldsymbol{J}\omega + T \tag{4.1.3}$$

$$\dot{q} = \frac{1}{2}\boldsymbol{\Omega}(\omega)q \tag{4.1.4}$$

where $J$ is the Moment of Inertia matrix, $\omega$ is the angular velocity of the body relative to the inertial frame, $\boldsymbol{T}$ is the applied total body torque, $\boldsymbol{q}$ is the quaternion, and

$$\boldsymbol{\Omega}(\omega) = \begin{bmatrix} -[\omega \times] & \omega \\ -\omega^T & 0 \end{bmatrix} \tag{4.1.5}$$

$$[\omega \times] = \begin{bmatrix} 0 & -\omega_3 & \omega_2 \\ \omega_3 & 0 & -\omega_1 \\ -\omega_2 & \omega_1 & 0 \end{bmatrix} \tag{4.1.6}$$

The translational motion of a rigid vehicle is determined by the external forces acting on the center of mass of the body. Again, using Newton's second law, the translational acceleration is due to the external body forces,

$$a_{BF} = {}^{F_B}/_{m_{FSP}} \tag{4.1.7}$$

Where $F_B$ is the total external body forces acting on the FSP. In an inertial coordinate system the total acceleration also accounts for the gravitational forces. The gravitational force acting between two masses, from Newton's law of gravity, is expressed as,

$$F_g = G\frac{Mm}{\|r\|^2}\hat{\boldsymbol{u}}_r \tag{4.1.8}$$

where

$$\hat{\boldsymbol{u}}_r = \frac{\vec{r}}{\|r\|} \tag{4.1.9}$$

from these equations and using the relationship of relative two-body motion, the governing equation of motion of $M$ relative to $m$ is,

$$\ddot{\vec{r}} = -\frac{G(M+m)}{\|r\|^3}\vec{r} \tag{4.1.10}$$

since the mass of the sphere, $m$, is much smaller than that of the earth, $M$, it can be neglected so that

$$\ddot{\vec{r}} = -\frac{\mu}{\|r\|^3}\vec{r} \tag{4.1.11}$$

where the gravitational parameter $\mu$ is defined as:

$$\mu = GM \tag{4.1.12}$$

and *r* is the position vector between the two masses *M* and *m*, being the earth and the Falling Sphere Probe, respectively.

Then the total acceleration of the FSP as seen from an inertial frame is,

$$a_I = a_{BF} + \ddot{\vec{r}} = {}^{F_B}/_{m_{FSP}} - \frac{\mu}{\|r\|^3}\vec{r} \tag{4.1.13}$$

Under the assumption of an inviscid, irrotational flow outside the boundary layer, the continuity and momentum equations are respectively,

$$\frac{\partial \rho}{\partial t} + (V \cdot \nabla)\rho + \rho \nabla \cdot V = 0 \tag{4.1.14}$$

$$\frac{\partial V}{\partial t} + \nabla\left(\frac{1}{2}\mathrm{V}^2\right) + \frac{\nabla P}{\rho} + \mathrm{F_{body}} = 0 \tag{4.1.15}$$

Where $F_{body}$ represents the body forces (per unit volume), which in this case is a gravitational force.

**B. Mission Objectives**

Measurements with the Falling Sphere Probe, FSP, will be used to directly determine atmospheric density and wind profiles. The 3-axis accelerations measured by the sphere have two contributions, namely a contribution due to the atmospheric density and a contribution due to the atmospheric winds. In order to make the analysis tractable, two assumptions are made, namely that the vertical winds are negligible and the horizontal winds are uniform across the distance separating the upleg and downleg portion of the trajectory. With those assumptions, a sphere that is moving vertically will experience a vertical acceleration related to the atmospheric density and horizontal accelerations related to the horizontal winds. In reality, the sphere motion has both vertical and horizontal components and the accelerations will have contributions from both density and wind effects. The data analysis requires a solution for all of the unknown parameters simultaneously, which can be done in a straightforward manner. The density profile will be determined by the equation for the atmospheric drag force in a given direction, which for this case is the z-component of the measured acceleration. Taking Eq. (4.1.1) and solving for the density yields,

$$\rho_\infty = \frac{2ma_D}{C_D V^2 A_{ref}} \tag{4.2.1}$$

where m is the mass of the sphere, $a_D$ is the drag acceleration, $\rho_\infty$ is atmospheric density, $V_\infty$ is the velocity component in that direction relative the background atmosphere, $C_D$ is the drag coefficient, and $A_{ref}$ is the cross-sectional area of the sphere.

### C. Mathematical Model

To simulate the expected response from the system, a Simulink/Matlab model was developed using the governing equations of motion. The model has the capability of forcing the sphere with randomly generated wind velocities to create an accelerometer signal output. The output is then taken, and the model backs out the wind velocities that caused the accelerations and is compared to the initial wind velocity (ones that were randomly generated).

Because of the complexity of the model, several assumptions are made to simplify the systems to something solvable. From the estimation of the rocket trajectory and profile, the sphere will be assumed to be at high velocities for the entire flight. Because the sphere is not completely smooth on its outer surface, i.e. there are many screw heads, seams, divots, and the majority of the surface is a fiberglass composite, the flow will be considered turbulent during the entire flight. This will be verified by the Reynolds number, *Re*. Flows with Re > $5 \times 10^5$ are considered turbulent flow, ref [9].

### D. Initial Conditions & Inputs

The simulation starts the time of ejection, $t_{eject} = 70.0\ seconds$. Several initial conditions must be known to start the simulation. The initial position is the Wallops Flight Facility (WFF) launch pad. The given latitude, $\phi = 37.48^o$, longitude, $\lambda = -75.48^o$, and altitude, $h = -0.021\ m$, of the launch pad allow for the calculation of the *X, Y, Z* coordinates in Earth Centered Fixed (ECF) frame according to ref[8] as,

$$X_{ECF} = [N(\phi) + h]\cos(\phi)\cos(\lambda) \tag{4.4.1}$$

$$Y_{ECF} = [N(\phi) + h]\cos(\phi)\sin(\lambda) \tag{4.4.2}$$

$$Z_{ECF} = [N(\phi)(1 - e^2) + h]\sin(\phi) \tag{4.4.3}$$

where *N* is the length of the normal to the ellipsoid given by,

$$N(\phi) = \frac{a}{\sqrt{1 - e^2 sin^2(\phi)}} \tag{4.4.4}$$

where according to the WGS 84 model, the earth's semi-major axis, $a = 6378.137\ km$, and the eccentricity of earth's ellipsoid, $e = 0.0818$.

The estimated position of the launch vehicle (Terrier Mk70-Improved Orion) at the ejection time is an altitude, $h_{Terrier} = 82.2\ km$, a range, $R_{terrier} = 26.7\ km$, an elevation angle, $El = 68.2^o$, and an azimuth angle, $Az = 115^o$. From this the estimated initial position at the time of ejection is, from methods used in ref [10], is

$$X_{0,ECF} = 2.357E^6\ m \tag{4.4.5}$$

$$Y_{0,ECF} = -4.567E^6\ m \tag{4.4.6}$$

$$Z_{0,ECF} = 3.901E^6\ m \tag{4.4.7}$$

The initial quaternion is calculated from the initial position vector of the launch facility and the known initial azimuth and elevation angles, and rail orientation. This is discussed in more detail in §FLIGHT DATA & TEST RESULTS.C: Flight Nutation & Precession

The initial inputs of the physical properties of the sphere were measured on the flight ready spheres. The method of these measurements is discussed in §BALANCING. These consisted of the center of mass, *CM*, the inertia tensor, *J*, the physical dimensions and mass.

**E. Aerodynamics**

Because the sphere is moving through the air, as well as spinning, the aerodynamic forces and moments need to be calculated. The aerodynamic forces and moments accounted for in this model are the drag forces, the Magnus force, and the torques caused from those drag forces on the surface of the sphere.

*1. Lift and Drag Coefficients*

The sphere is assumed to have an initial spin at a rate of 2 Hz. For a spinning sphere at this rate in an ideal flow, the lift coefficient is approximately, $C_L \approx 0.036$ at a Reynolds number (Re) of $8.2 \times 10^6$. For this simulation, the lift coefficient was assumed constant through the entire flight.

The drag coefficient, $C_D$, is a bit more complex. The majority of the flight is at supersonic speeds, except through the point of apogee, at which the velocity is transonic. The flow around the sphere, in terms of calculating the drag coefficient, is assumed to be turbulent the entire flight. The drag coefficient at high Mach numbers has many different parts. The components included in the model for a total drag coefficient are: pressure drag, skin friction drag, shockwave drag (for transonic and supersonic flows), and drag from excrescencies (holes, rivets, scratches, etc…)[11]. The total drag coefficient is the summation of coefficients expressed as,

$$C_{D;Total} = C_{D;P} + C_{D;f} + C_{D;SW} + C_{D;Ex} \tag{4.5.1}$$

The equations to model the various drag coefficients come from empirical data, based on rocket testing and performance characterization[11]. The pressure drag, $C_{D;P}$, was assumed to be a constant value of 0.2, as is reported in [12], and many other texts, for turbulent flow around a sphere. In calculating the drag due to skin friction, the roughness factor was assumed to be 0.0012 inches, the average surface finish to machined fiberglass composites [13].

*2. Aerodynamic Forces*

The aerodynamic forces include the drag force and the Magnus force. The drag force, $F_D$, is parallel to the freestream velocity and opposes the direction of flight. The drag force is simply calculated as,

$$F_D = \frac{1}{2}\rho_\infty C_{D,Total} V_\infty^2 A_{ref} \hat{\boldsymbol{\imath}}_{V_{FSP}} \tag{4.5.2}$$

where $A$ is the frontal area of the sphere, and $\hat{\boldsymbol{\imath}}_{V_{FSP}}$ is the unit vector in the direction of the velocity of the sphere.

The Magnus force is the lift produced by the rotation of the spinning sphere. The lift is in the direction of the cross product between the velocity vector and the spin axis. The rotation rate and the surface roughness affect the lift and drag coefficients. The force due to rotation is,

$$F_M = F_L(\omega \times v) = \frac{1}{2}\rho_\infty C_L V_\perp^2 A_{ref} \hat{\boldsymbol{\imath}}_{F_M} \tag{4.5.3}$$

where $V_\perp$ is the velocity perpendicular to the axis of rotation, and$\hat{\imath}_{F_M}$ is the unit vector in the direction of the cross product, expressed as,

$$\hat{\boldsymbol{\imath}}_{F_M} = \frac{\left(\hat{\boldsymbol{\imath}}_{\omega_{FSP}} \times \hat{\boldsymbol{\imath}}_{V_\perp}\right)}{\left\|\left(\hat{\boldsymbol{\imath}}_{\omega_{FSP}} \times \hat{\boldsymbol{\imath}}_{V_\perp}\right)\right\|} \tag{4.5.4}$$

Therefore the total external forces exerted on the rigid sphere, is the total body force as,

$$F_{BF} = F_D + F_M \tag{4.5.5}$$

*3. Aerodynamic Moments*

The only torques acting on the sphere are the aerodynamic moments. These are the moments due to the skin friction drag force acting on the surface of the sphere and the pressure drag force acting at the center of pressure of the sphere. (The moment caused by the umbi cords disconnecting will be neglected.) The moment arm to the skin friction drag is the radius of the sphere, which is approximately, $r_{FSP} = 6.125"$ (it is approximate because the outer components do not make a perfect 3D sphere). The moment arm to the pressure drag force is the distance from the center of pressure, $x_{cp}$, to the center of mass, $x_{cm}$. The center of mass is a physical measurement described in § BALANCING, the distance, $x_{cp}$, is calculated as,

$$x_{cp} = -\frac{1}{2} r \hat{\imath}_{F_{D;P}} \tag{4.5.6}$$

Then the torque acting on the body can be expressed as,

$$T_B = x_{cp} \times F_{D;P} + T_{F_{D;f}} \tag{4.5.7}$$

where $r$ is the sphere radius, $F_{D;P}$ is the drag force due to pressure drag, $\hat{\imath}_{F_{D;P}}$ is the unit vector in the direction of the drag force due to pressure drag, and $T_{F_{D;f}}$ is the torque caused by the drag force due to skin friction,

$$T_{F_{D;f}} = -F_{D;f} r_{FSP} \hat{\imath}_{\omega_{FSP}} \tag{4.5.8}$$

**F. Rotational and Translational Dynamics**

The attitude of the sphere is determined by simply integrating the governing equations of motion, Eq. (4.1.3) and Eq.(4.1.4), with respect to time. The integration is handled using a Simulink integration block. Integrating $\dot{\boldsymbol{\omega}}$ gives the rotation axis, and integration of $\dot{\boldsymbol{q}}$ gives the quaternion describing the orientation of the sphere from body coordinates to inertial coordinates. The applied torques and disturbance torques

acting on the system must be known. It is assumed that there is no applied torques, given that this is a free falling system, and the disturbance torques is estimated from the drag forces acting on the surface of the sphere. The quaternion also must be normalized as,

$$q_I^B = \frac{q_I^B}{\sqrt{(q_I^B)^T q_I^B}} \tag{4.6.1}$$

From the quaternion, a Direction Cosine Matrix, *DCM*, to rotate from Inertial to Body coordinates can be developed [14],

$$\boldsymbol{R}_I^B = \begin{bmatrix} q_1^2 - q_2^2 - q_3^2 + q_4^2 & 2(q_1q_2 + q_3q_4) & 2(q_1q_3 - q_2q_4) \\ 2(q_1q_2 - q_3q_4) & -q_1^2 + q_2^2 - q_3^2 + q_4^2 & 2(q_2q_3 + q_1q_4) \\ 2(q_1q_3 + q_2q_4) & 2(q_2q_3 - q_1q_4) & -q_1^2 - q_2^2 + q_3^2 + q_4^2 \end{bmatrix} \tag{4.6.2}$$

The translational dynamics are also a simple integration of the governing equation of motion, Eq.(4.1.13).

**G. Accelerometer Response**

The acceleration is calculated as seen for each of the six science accelerometers. This acceleration includes any translation acceleration and any acceleration due to rotations about any axis. The results of the rotation rate from the previous section will be used in determining the accelerations of the sphere. The accelerometers measure any acceleration in the direction of the axis of the device. Each accelerometer may see translational accelerations and centripetal accelerations. The translational acceleration is found from the aerodynamic body forces (as described above) acting on the sphere is given by Eq. (4.1.7), and the centripetal acceleration is expressed as,

$$a_c = -\omega_B^2 r \tag{4.7.1}$$

where, *r*, is the perpendicular distance from the accelerometer to the axis of rotation.

It is assumed that the measuring device is at the middle of the accelerometer housing. The channels of the accelerometers are shown in Figure 2. The acceleration of each channel is calculated as follows in matrix form,

$$A_{ch} = \boldsymbol{C}X \tag{4.7.2}$$

where $A$ is the vector of all the channel measurements, $X$ is the state variable vector, and $\boldsymbol{C}$ is the matrix of coefficients, defined as,

$$A_{ch} = [a_{chan1} \quad a_{chan2} \quad a_{chan3} \quad a_{chan4} \quad a_{chan5} \quad a_{chan6}]^T \tag{4.7.3}$$

$$X = \begin{bmatrix} a_x & a_y & a_z & \omega_x^2 & \omega_y^2 & \omega_z^2 \end{bmatrix}^T \tag{4.7.4}$$

$$\boldsymbol{C} = \begin{bmatrix} \cos(\alpha) & \sin(\alpha) & 0 & -r_{vert} & -r_{horz} & -r_{angled} \\ -\cos(\alpha) & -\sin(\alpha) & 0 & -r_{vert} & -r_{horz} & -r_{angled} \\ 0 & 0 & 1 & -h_{vert} & 0 & -h_{vert} \\ 0 & 0 & -1 & -h_{vert} & 0 & -h_{vert} \\ 0 & -\sin(\alpha) & \cos(\alpha) & -r_{angled} & -r_{horz} & -r_{vert} \\ 0 & \sin(\alpha) & -\cos(\alpha) & -r_{angled} & -r_{horz} & -r_{vert} \end{bmatrix} \tag{4.7.5}$$

Then solving for the state variable,

$$X = \boldsymbol{C}^{-1} A_{ch} \tag{4.7.6}$$

where the distances $r$ and $h$ are measured from the CG to the point of measurement in the accelerometer. For the angled mounted accelerometers, $r_{vert}$is the vertical offset, $r_{horz}$ is the horizontal offset, and $r_{angled}$ is the total distance. For the vertically mounted accelerometers, $h_{vert}$ is the vertical offset.

The results in Eq. (4.7.6) give the x, y, and z axes accelerations and rotation rates in the sphere body coordinates. A simple rotation will change the results from the sphere coordinates into ECI coordinates.

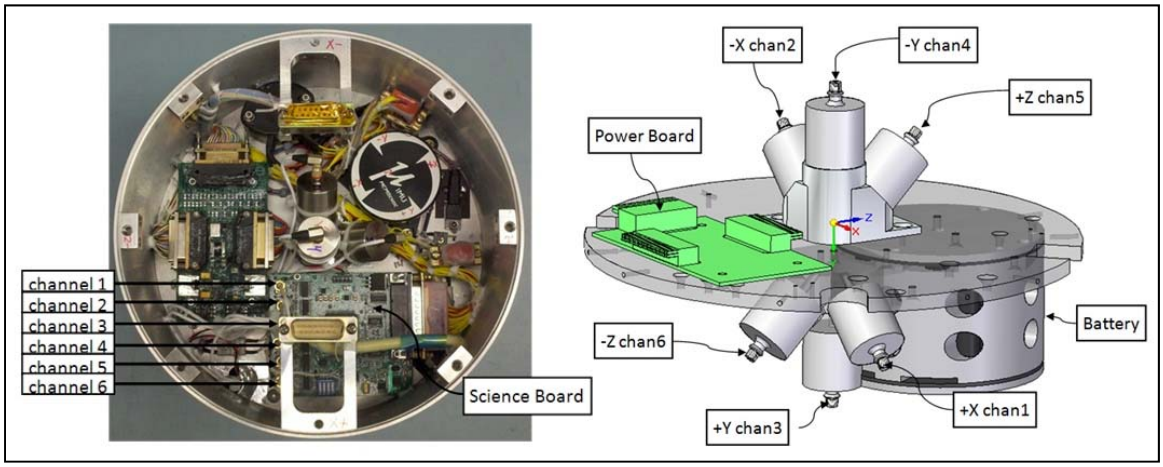


**Figure 2: Accelerometer Channels**

Using the manufacturer's specifications (see appendix), appropriate errors were added into the accelerometer signals in the simulation. These errors include position error, sensitivity error or scale factor, bias, and white noise.

# OVERALL DESIGN

## A. Sensors

The FSP structure (see Figure 3) is a 31.115 cm (12.25 in) sphere that is comprised of two dielectric material halves. The composite material shell ensures strength while minimizing mass and creates a "transparent" RF window for the telemetry and GPS antenna. An internal "can" with a deck-plate (see Figure 4) will serve as the mounting platform and faraday cage for two symmetrical ultrasensitive 3-axis accelerometer systems (the wind measurement sensors), an IMU that includes a less sensitive 3-axis accelerometer, gyros, and magnetometer for precise attitude determination, a GPS unit for accurate payload trajectory tracking, signal conditioning and encoding electronics, a S-band transmitter, and power switching/distribution system electronics. A 22.9 cm outer diameter, combination S-band/GPS antenna ring encircles the can. Except for the ultra-sensitive accelerometers, these components are all systems commonly used by NSROC for sounding rocket missions. The layout of the internal components is illustrated in Figure 5. The deckplate components are placed to optimize balance of the sphere and maximize spin-stability about the z-axis. All unnecessary material in the can and deck plate is removed to reduce the mass as much as possible.

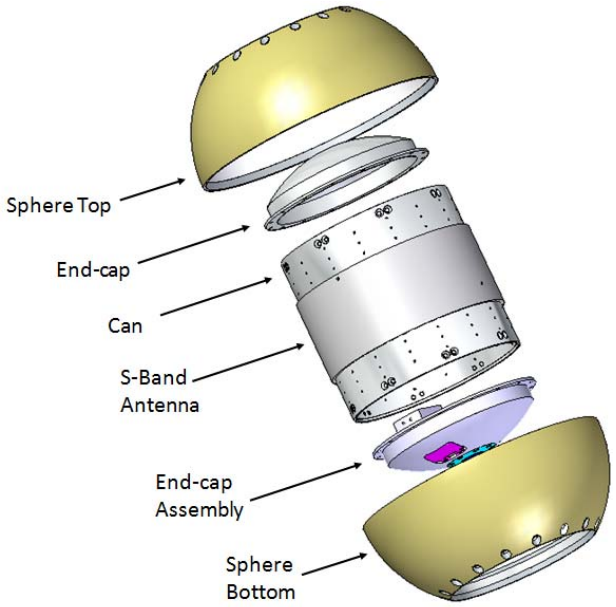


**Figure 3: Sphere Make-up**

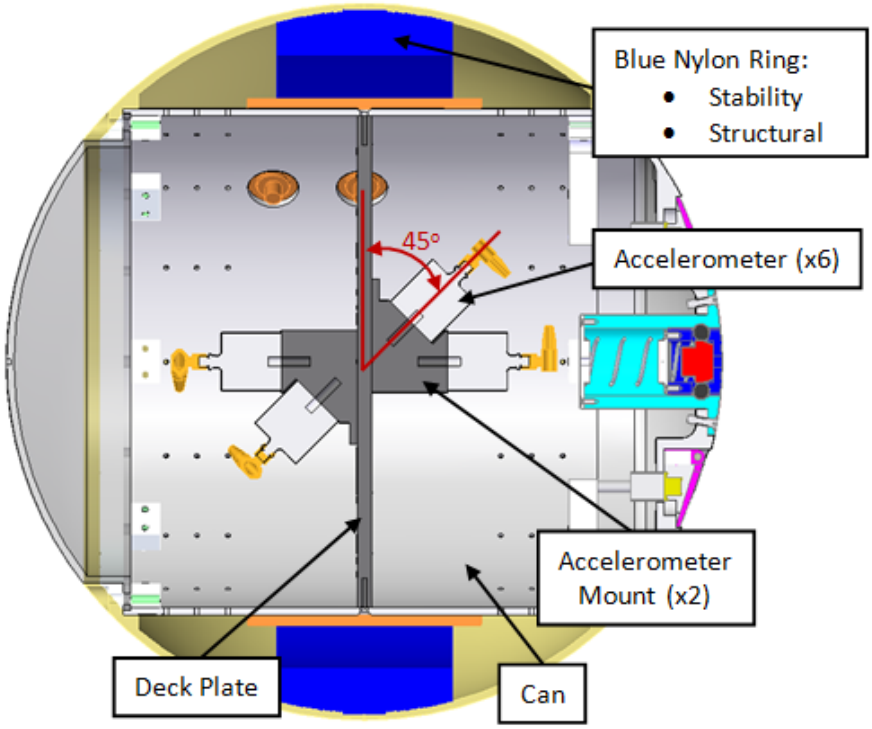


**Figure 4: Internal Can and Accelerometer Mounts**

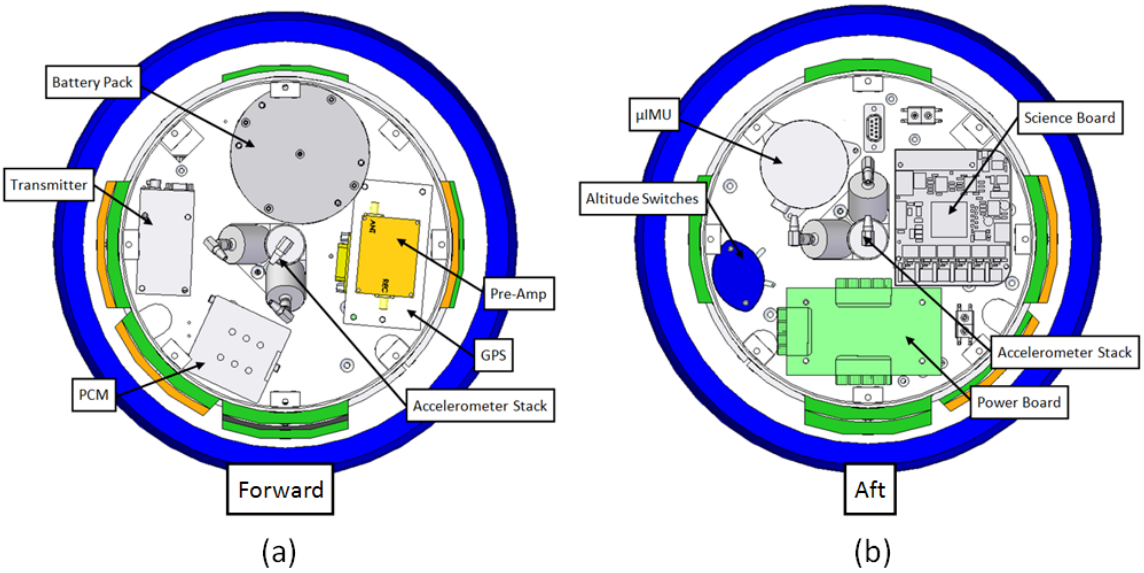


**Figure 5: Sphere Internal Layout**

The ultra-sensitive 3-axis accelerometer systems are comprised of three commercially available single-axis piezoelectric accelerometer devices. Each single-axis device is a 3.6 x 2.5 cm cylinder that is sensitive along the major axis. The 3-axis systems are completed by configuring three single-axis devices such that one single-axis device is positioned for sensitivity in each of the x, y, and z axes (see Figure 5 and Figure 6). One3-axis accelerometer system is mounted on the top side of the deck-plate, with another system mounted directly below the deck-plate (see Figure 6). This configuration provides symmetry for removing the biases due to the offsets from the sphere center in the single-axis accelerometer device locations within the dual 3-axis configurations. The mounting fixture is designed to minimize the distance the two angled accelerometers are from center. Being off-center introduces centripetal accelerations in the measurements that must be accounted for.

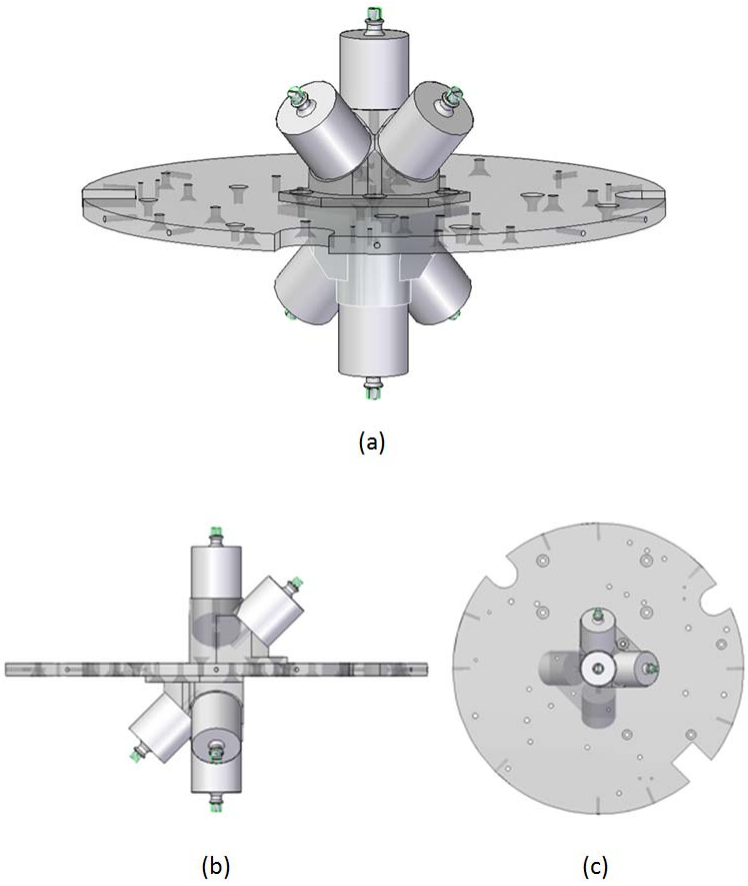


**Figure 6: Accelerometer Orientation**

## B. Structure/ Attitude Control

The Falling Sphere Probe is a spin-stabilized object with a spin rate of about 2 Hz. In order to be stable the sphere has to be a major axis spinner. That is, the angular velocity vector of the sphere must lie in the direction of its major axis of inertia. For the coordinate system shown in (Figure 7), this means that the sphere must spin about the y-axis. Because the sphere has no active control system, the stability of the sphere relies on the inertia tensor and is said to have a passive attitude control system. The easiest way to be a major axis spinner, or oblate spinner [10], is to be "short and fat". Since the sphere is symmetrical and

rigid, it cannot be short or fat. The control is then maintained by the physical geometry of the sphere, or more so, what's inside the sphere and how it is placed.

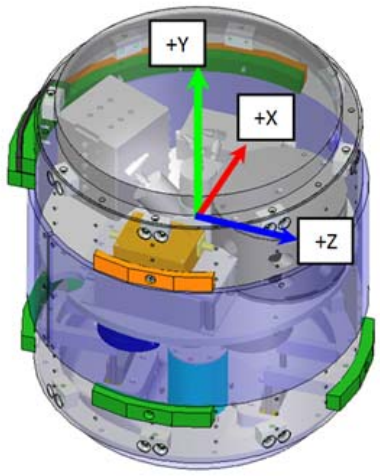


**Figure 7: Sphere Coordinate System**

The system internally is "tall and skinny", as seen by the "can" assembly, and therefore the sphere naturally wants to be a minor axis spinner, or a prolate spinner [10]. A spacecraft that is a minor axis spinner with no active attitude control is considered to be unstable. To avoid this and make it a major axis spinner, a ring was put around the equator of the "can". To not interfere with the antenna, the material of this ring had to be non-metallic. The ring was made of nylon and has a second purpose of joining the two dielectric halves of the sphere together. With this radially outward as far as possible from the center and at the equator, it created a spinning top-like object, making it a major axis spinner. The modeled stabilizing ring and an actual ring are shown in Figure 8.

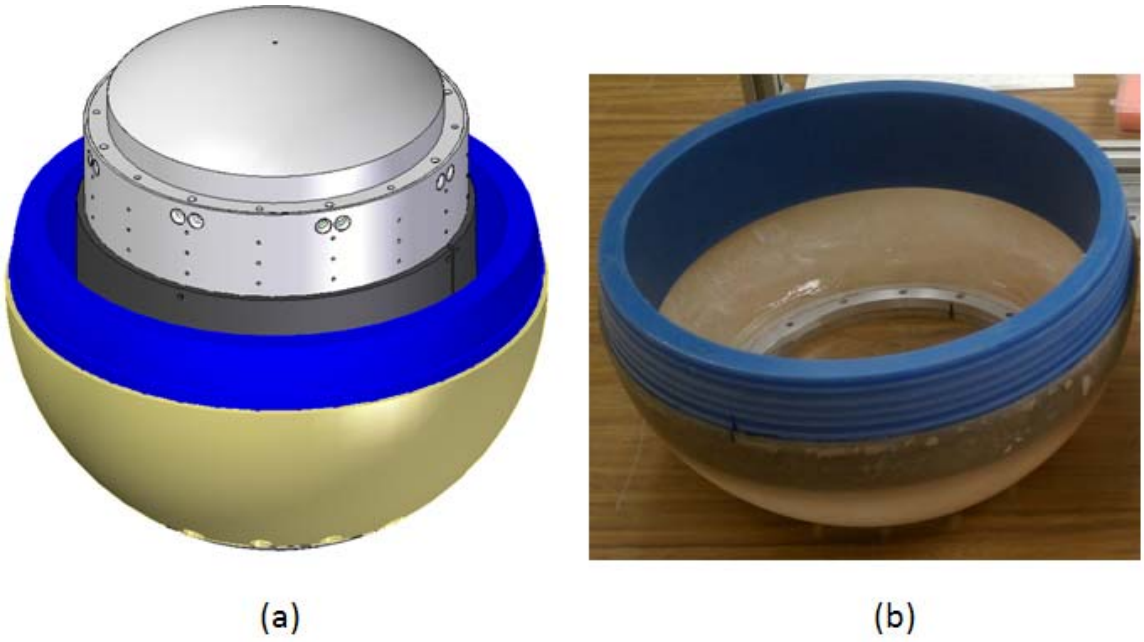


**Figure 8: Stabilizer/Joiner Ring**

# BALANCING

To maintain stability of the sphere and not saturate the instruments on board, the orientation of the spin needs to be as constant as possible. The goal is to reduce the wobble of the sphere. This is done with the center of mass (CM) and the moments of Inertia (MOI). For the sphere to spin perfectly about its center axis, the CM would have to be located somewhere on the spin axis, and the Inertia tensor would have no products of Inertia (POI). When this is the case, the sphere is considered perfectly rotationally balanced.

## A. Center of Mass (CM)

### *1. Concept and Ability*

In order to have the center of mass lie somewhere along the spin axis, or the y-axis (ideally, they are one and the same), there needs to be a way of changing the CM after all the components are installed including all the wiring harnesses. The method chosen was to use large weights (8-24grams) that attach to the outside of the can for "rough" balancing and to attach small weights (0.02-0.13 oz) the outer hemispheres for fine tuning to shift the CM to the desired location. Three different sizes of the large weights were used to vary the ability in "rough" balancing the sphere. They varied in thickness, but the dimensions were the same, allowing the weights to be stacked in various patterns to achieve the desired weight at a specific location. Since these larger weights are attached to the can, the sphere has to be opened, meaning the dielectric hemispheres have to be removed. The small weights are fasteners of two different material types, Aluminum and Stainless Steel, varying in lengths to give a varied of weights. The small weights are placed in locations around the encaps of the spheres. This allows for a "fine tuning" without having to change the final assembly of the sphere, the CM is adjusted in the flight configuration. The two kinds of weights used are shown in Figure 9below.


**Figure 9: Balancing Weights**
**a) Large weights for "rough" balancing, b) Small weights for "fine tuning"**

Adjusting the CM to the desired location was an iterative process. The sphere would be weighed and the CM would be calculated. Based on the results counter weights would be attached and the sphere re-weighed and the CM re-calculated. This process would repeat until the difference between iterations was less than the contribution of the smallest weight available per stage. The CM balancing had to occur in two stages. The first stage is the "rough" balancing stage, using the large weights. As mentioned above, in order to attach the large weights, the sphere was opened. This required that all the adjustments to the CM with the large weights had to be done in one stage. Once the maximum resolution was met in this stage, the next stage commenced. The second stage is the "fine tuning" of the sphere. In the joint between the encaps and the dielectric hemispheres there are 16 holes. Every other hole is used for structural purposes joining the hemisphere and the encap to the "can". The other 8 holes are tapped into the encap and are used for the "fine tuning". The application of the different stages is seen in Figure 10 below.

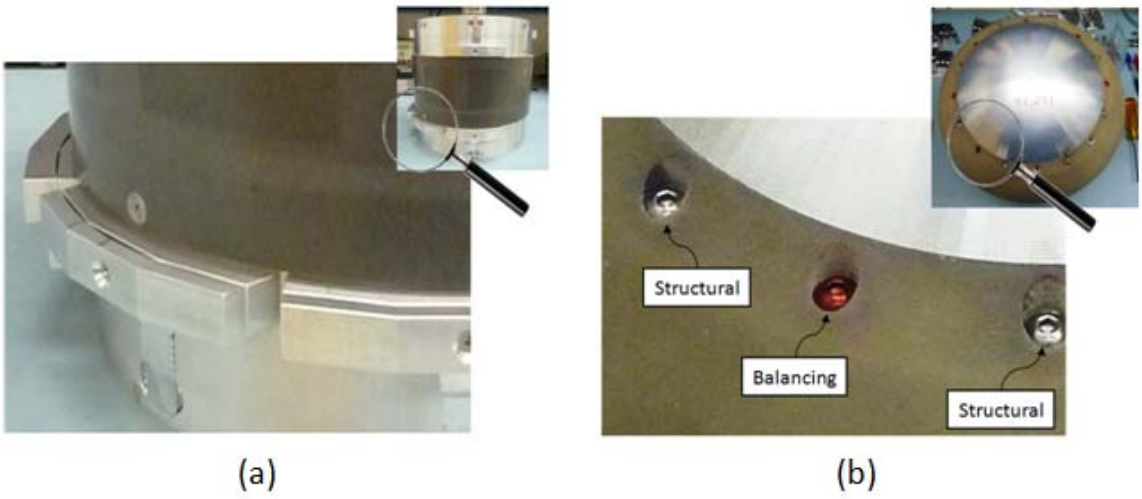


**Figure 10: Balancing Weights on Sphere**
**a) Large weights in stage 1, b) Small weights in stage 2**

The Multiple Point Weighing Method was used to calculate the CM and also the total mass of each sphere [15]. The method is to support a platform by at least three load cells, and the CM is calculated from the resultant moments caused by the forces at these cells, refer to Figure 11 below. The accuracy of this method is reported to only be moderate. Some of the inherent problems with this method are the introduction of side loading by linking the load cells together with a platform and the deformation of the platform itself when under the load of the object being measured [16].

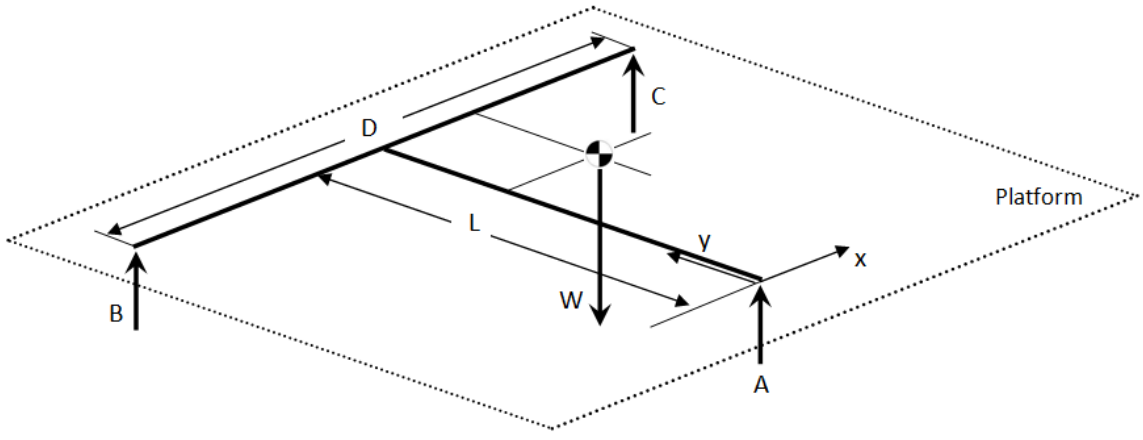


**Figure 11: Multiple Point Weighing Method**

The total weight of the measured object is simply the summation of the forces:

$$\mathrm{W} = \mathrm{A} + \mathrm{B} + \mathrm{C} \tag{6.1.1}$$

The calculation of the center of mass is done by taking the moments about point A:

$$\Sigma M_x = (\mathrm{B} + \mathrm{C})L - \mathrm{W}x = 0 \tag{6.1.2}$$

$$\Sigma M_y = \mathrm{W}y + \frac{\mathrm{D}}{2}(\mathrm{B} - \mathrm{C}) = 0 \tag{6.1.3}$$

$$x = \frac{(\mathrm{B} + \mathrm{C})L}{\mathrm{W}} \tag{6.1.4}$$

$$y = \frac{\mathrm{D}}{2\mathrm{W}}(\mathrm{C} - \mathrm{B}) \tag{6.1.5}$$

The presence of side loading in the system introduces large errors in the measurement results. To eliminate this error, the platform is not attached to the load cells, but floats on top. This is accomplished using kinematic mounts, where the first ball makes contact with the frame at exactly three points (a sphere in a trihedral, or cone for simplicity), the second ball at two (a sphere in a V-groove), and the third ball at just one (a sphere on a flat surface).These six points of contact exactly constrain the six degrees of freedom of the platform. This mounting technique is illustrated in Figure 12,

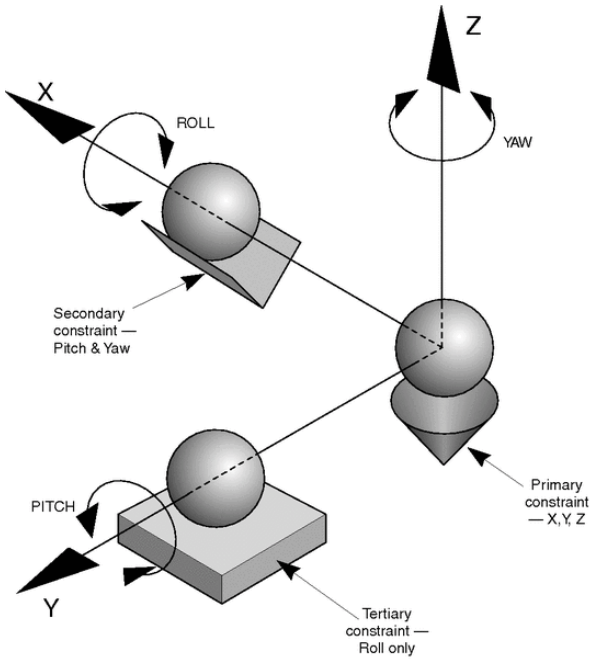


**Figure 12: Kinematic Constraint (Courtesy of Newport Corpration)**

To reduce the error caused by the platform deformation, the thickness of the platform was increased to support loads up to 10 kg (including test fixtures).

*2. Falling Sphere Probe CM Measurements*

In order to get accurate measurements of the sphere the table platform and all fixtures used in the process had to be calibrated. The calibration process included using an object with a precisely known weight and center of mass. A high precision 3 inch steel ball bearing was used as the calibration object. The accuracy of the CM table was good to less than ½ mm. The fixtures had to allow for the sphere to be oriented in the 3 different x, y, and z axes, as well as allow the sphere to be removed from the table as part of the measuring procedure.

For each orientation and every balance weight configuration, fifteen measurements were recorded. As mentioned earlier, the rough balancing had to take place first. Figure 13 shows the rough balance setup in two configurations: a) shows the orientation for measurements for the CM in the x-y plane, and b) shows

the orientation for measurements in the x-z plane. Measurements in the y-z plane are taken in an orientation rotated +90 degrees around the horizontal axis from that shown in Figure 13:(a).

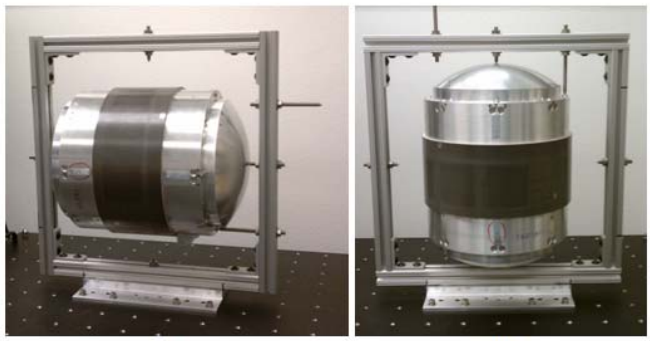


**Figure 13: CM Measurements: Rough Balancing**
**a) CM measurements in the x-y plane, b) CM measurements in the x-z plane**

Once the rough balance is complete, the outer shells (dielectric hemispheres) are put in place and the sphere has to be re-balanced in its final configuration. This process is illustrated in Figure 14for a couple of orientations. FIG (a) shows the setup for measuring in the x-y plane, (b) is measuring in the x-z plane. Measurements in the y-z plane are taken in an orientation rotated +90 degrees around the horizontal axis from that shown in Figure 14: (a).

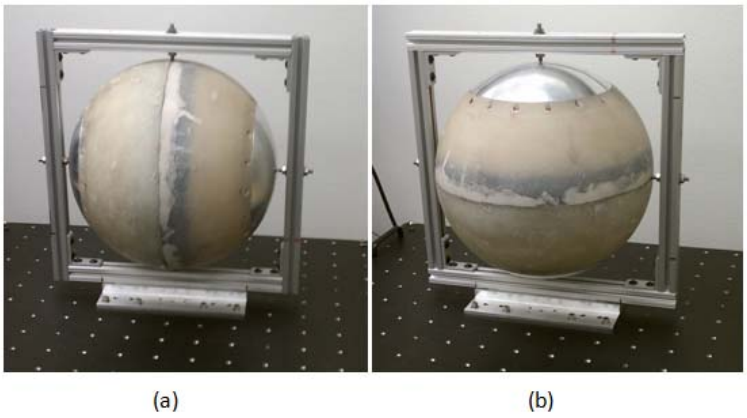


**Figure 14: CM Measurements: Fine Tuning**
**a) CM measurements in the x-y plane, b) CM measurements in the x-z plane**

The final CM measurement results are shown below in Table 1.In calibrating the table, the geometric center of the fixture, and consequently the geometric center of the sphere are known. The values in the table reflect the deviation from the geometric center of the sphere.

**Table 1: Final CM Position of Falling Sphere Probes (y-axis == spin axis)**

| Sphere: 41.090 | | | | | Sphere: 41.091 | | | |
|---|---|---|---|---|---|---|---|---|
| | Mass [kg] | dx [mm] | dy [mm] | dz [mm] | mass [kg] | dx [mm] | dy [mm] | dz [mm] |
| Mean | 9.645 | -0.014 | -0.020 | 0.040 | 9.833 | -0.096 | -0.037 | -0.078 |
| std Dev | 0.0095 | 0.060 | 0.098 | 0.060 | 0.0095 | 0.060 | 0.098 | 0.060 |

## B. Moments of Inertia (MOI)

### *1. Concept and Ability*

Since the capability of measuring the products of inertia on a typical spin balance machine is not available in the lab, the method of measuring the moments and products of inertia is by oscillating the object on a torsion pendulum. This method consists of measuring the oscillation period of the object of interest and then calculates the inertia of the axis of rotation.

The centrifugal and windage forces exerted on the sphere are neglected because the sphere moves very slowly during this kind of measurement. The entrapped and entrained air effects will also be neglected due to the sphere having a much higher density than air. Also the sphere has sufficient structural integrity so as to not deflect due to the oscillation motion. Typically the total number of MOI measurements made is nine: three in each of the three mutually perpendicular planes. However, since the coordinate axes are the intersections of these planes, then the MOI along these axes will be common in the two planes, thus reducing the total number to six measurements [17].The six oscillation measurements are about the body axes (X, Y, and Z) and about three axes at 45 degrees in each of the three planes, as shown in Figure 15.

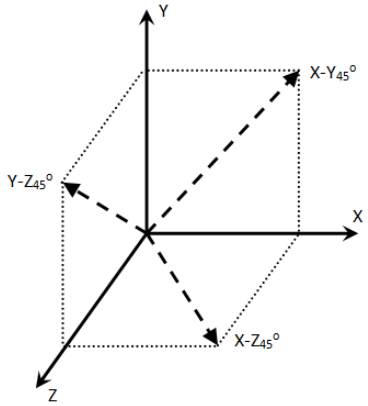


**Figure 15: MOI Measurement Axes**

Ideally the test fixture needs to be able to rotate the sphere into the six different orientations in such a way as to locate the CM on the axis of rotation of the machine; otherwise, the parallel axis theorem needs to be used. The fixture also needs to interface with the sphere with as little or no alteration of the final flight configuration of the sphere. Two separate fixtures were used to orient the sphere into the six different configurations, one fixture per 3 axes of rotation. The fixtures are shown in Figure 16below.

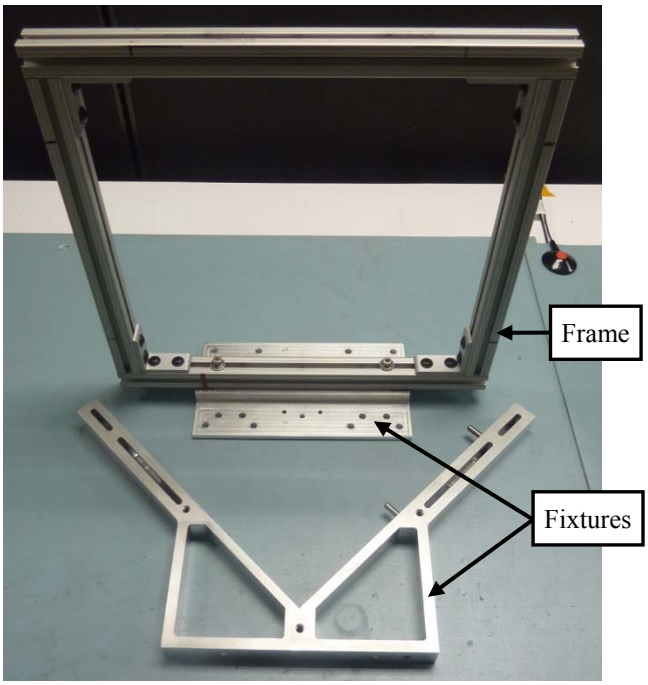


**Figure 16: MOI and CM Test Fixtures& Frame**

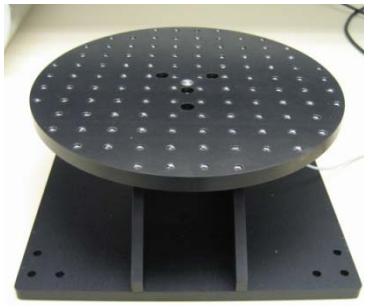

**Figure 17: Oscillating Table for MOI measurements**

To calculate the MOI, an oscillating table (shown in Figure 17above) is used to measure the period of oscillation. If the table is rotated by an angle, $\varphi$, then the restoring torque acting on the system is,

$$\tau = -k\varphi \tag{6.2.1}$$

where *k*, is a constant of the oscillatory table, which has to be measured. With an object of interest on the table, the oscillation frequency will have the response of

$$\omega_O = \sqrt{\frac{k_O}{I_O}} \tag{6.2.2}$$

where $\omega_O$ is the oscillation frequency in rad/s, $k_O$ is the effective stiffness constant, and $I_O$ is the total inertia of entire system. The frequency can also be expressed in terms of its period,

$$\omega_O = 2\pi f = \frac{2\pi}{T_O} \tag{6.2.3}$$

Therefore, the oscillation in terms of the measured period and the inertia is, combining Eqs. (6.2.2) and (6.2.3),

$$\frac{2\pi}{T_O} = \sqrt{\frac{k_O}{I_O}} \tag{6.2.4}$$

solving for the spring constant yields,

$$k_O = \left(\frac{2\pi}{T_O}\right)^2 I_O \tag{6.2.5}$$

With two independent period measurements, one with the bare table and one with an object of a known moment of inertia, the table constants *k* and *I* can be determined. The object used to calibrate the system is a2 inch precision steel ball bearing. Since *k* = *constant*, using Eq. (6.2.5) above for two measurements,

$$\left(\frac{2\pi}{T_{calibrate}}\right)^2 I_T = k_{table} = \left(\frac{2\pi}{T_{table}}\right)^2 I_{table} \tag{6.2.6}$$

where,

$$I_T = I_{table} + I_{calibrate} \tag{6.2.7}$$

Then,

$$I_{table} = \frac{\left(\frac{T_{table}}{T_{calibrate}}\right)^2 I_{calibrate}}{1 - \left(\frac{T_{table}}{T_{calibrate}}\right)^2} \tag{6.2.8}$$

Simplifies to,

$$I_{table} = \frac{T_{table}^2 I_{calibrate}}{T_{calibrate}^2 - T_{table}^2} \tag{6.2.9}$$

Using Eq. (6.2.9) in Eq.(6.2.5), the table constant is expressed as,

$$k_{table} = \left(\frac{2\pi}{T_{table}}\right)^2 I_{table} = \frac{4\pi^2 I_{calibrate}}{T_{calibrate}^2 - T_{table}^2} \tag{6.2.10}$$

and the inertia about the axis of rotation of the object of interest can be expressed in terms of known fixture inertias and measured oscillation periods as,

$$I_{object} = k_{table}\frac{T_{total}^2}{4\pi^2} - I_{total;setup} = \frac{I_{calibrate} T_{total}^2}{T_{calibrate}^2 - T_{table}^2} - I_{total;setup} \tag{6.2.11}$$

where,$I_{total;setup}$is the combined inertias of all items except the object of interest, about the rotation axis. This includes: the table, fixtures, and frames used to orient the sphere along the proper axis alignment. These inertias are estimated from precise CAD models and known weights of each item.

Once the inertia has been measured about all six axes, the Products of Inertia (POI) can be determined. The inertia about the axes oriented some angle, $\vartheta$, off the principle axis and lying in a plane formed by two

adjacent principle axes, is not the product of inertia for the object. The measured axis will be denoted by, $I_A$and is related to the POI through the equation [17],

$$I_{Axy} = I_{yy}sin^2(\vartheta) + I_{xx}cos^2(\vartheta) - P_{xy}\sin(2\vartheta) \tag{6.2.12}$$

where$P_{xy}$ is the Product of Inertia. Solving Eq. (6.2.12) for the product, given the inertia measurements,

$$P_{xy} = \frac{I_{yy}sin^2(\vartheta) + I_{xx}cos^2(\vartheta) - I_{Axy}}{\sin(2\vartheta)} \tag{6.2.13}$$

For the case where, $\vartheta$=*45*$^o$, Eq. (6.2.13) simplifies to, for the three products,

$$P_{xy} = \frac{I_{xx} + I_{yy}}{2} - I_{Axy} \tag{6.2.14}$$

$$P_{xz} = \frac{I_{xx} + I_{zz}}{2} - I_{Axz} \tag{6.2.15}$$

$$P_{yz} = \frac{I_{yy} + I_{zz}}{2} - I_{Ayz} \tag{6.2.16}$$

*2. Falling Sphere Probe MOI Measurements*

The MOI measurements were made on the oscillation table. The table uses a special suspension system custom designed and built by the Space Dynamics Laboratory. The design eliminates friction and stiction while minimizing the energy loss in the system. The period of oscillation was measured with a camera recording at 60 fps, giving the period a resolution of 0.0167 seconds. The setup simply measured the time between two tick marks on the table. A minimum of sixteen samples were taken for each measurement along each rotation axis. The sample mean and standard deviation are then calculated and the results used in determining the moments and products of inertia from Eq. (6.2.11) and Eqs. (6.2.14)-(6.2.16) above respectively.

Since the sphere has to be measured in six different orientations, and two different setups where used to achieve the proper orientation (see Figure 18), these setups have to be accounted for in the final measurement. Each setup, in its entirety minus the sphere, will have a different MOI. Because of this each setup has to be measured and the inertias calculated, using Eq. (6.2.11), so as to “tare” the system for that axis measurement. This was done for each orientation.

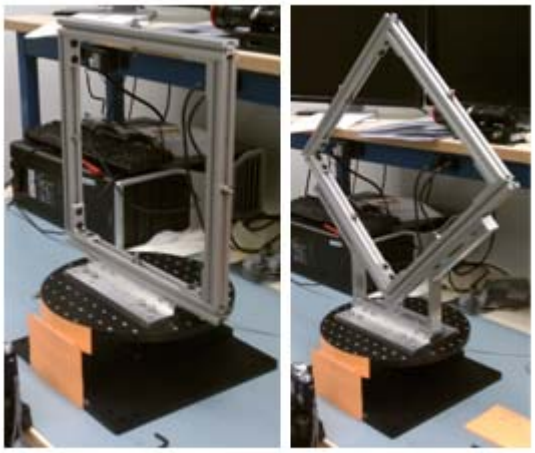


**Figure 18: MOI Setup Orientations**
**a) MOI Measurements along Principle Axes, b) MOI Measurements along 45$^{o}$ Axes**

Once all the fixture setup periods have been measured, the MOIs can then be measured in their six different orientations. The different orientations can be placed from various rotations of the sphere within one of the two fixtures. Three of the orientations are shown in Figure 19 below.

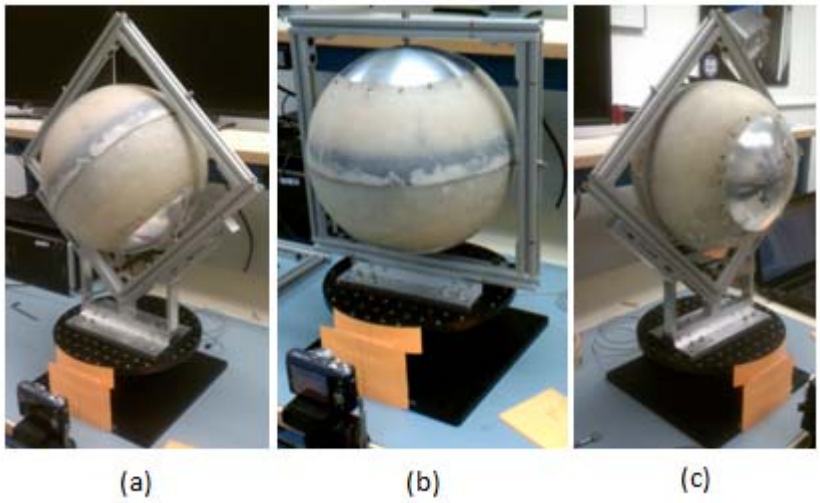


**Figure 19: MOI Measurement Orientations**
**a) MOI Measurements along 45$^{o}$ Axis, in X-Y plane**
**b) MOI Measurements along Principle Axis, Y-axis**
**c) MOI Measurements along 45$^{o}$ Axis, in X-Z plane**

The final measured MOIs, and calculated POIs are given in Table 2 below for both spheres. For a perfect spinner about the Principle axis, the products of inertia are zero. For these spheres, the products are not zero, but are considerably smaller than the MOIs.

**Table 2: Final MOI & POI of Falling Sphere Probes (y-axis == spin axis)**

| Sphere: 41.090 | | | | Sphere: 41.091 | | |
|---|---|---|---|---|---|---|
| Inertia Tensor [kg-m$^2$] | | | | Inertia Tensor [kg-m$^2$] | | |
| 0.093798 | 0.001191 | -0.000784 | | 0.096334 | 0.004425 | 0.001161 |
| 0.001191 | 0.104970 | 0.001972 | | 0.004425 | 0.105688 | 0.002567 |
| -0.000784 | 0.001972 | 0.096103 | | 0.001161 | 0.002567 | 0.093110 |

*3. Falling Sphere Probe Angle of Precession*

Since the products of inertia are not zero, the sphere will nutate as it spins. This change in orientation of the spin axis can be defined by the products of inertia and is called precession. The nutation angle,$\theta_n$, is calculated using the inertia tensor. Under the assumption of torque-free motion (neglecting secondary drag forces) the net moment about the center of gravity is zero. The angular momentum vector, $H_G$, is a vector fixed in inertial space. Let $H_G$ define the Z axis of the inertial frame as shown in Figure 20 below. The angle between the y-axis and $H_G$ is the nutation angle (Euler angle definition) [10]. Assuming the nutation angle remains constant, by definition,

$$cos(\theta_n) = \frac{H_G}{\|H_G\|} \cdot \hat{\jmath} \tag{6.2.17}$$

where the angular momentum is defined as,

$$H_G = \boldsymbol{I}\omega_s \tag{6.2.18}$$

$$H_G = \begin{bmatrix} 0.0963 & 0.0044 & 0.0012 \\ 0.0044 & 0.1057 & 0.0026 \\ 0.0012 & 0.0026 & 0.0931 \end{bmatrix} \begin{bmatrix} 0 \\ 4Hz \\ 0 \end{bmatrix} = \begin{bmatrix} 0.111 \\ 2.656 \\ 0.065 \end{bmatrix} \tag{6.2.19}$$

$$\hat{\imath}_{H_G} = \frac{H_G}{\|H_G\|} \tag{6.2.20}$$

solving Eq. (6.2.17)for the nutation angle, $\theta_n$,

$$\theta_n = \cos^{-1}\left(\hat{\imath}_{H_G} \cdot \hat{\jmath}\right) \approx 2.77° \tag{6.2.21}$$

The precession rate is expressed as,

$$\omega_P = \frac{mgr}{I\omega_s} \approx 0.90Hz \tag{6.2.22}$$

where $m$ is the mass of the sphere, $g$ is the gravity constant, $r$ is the distance from the pivot point to the center of gravity (which is also the radius of the sphere), $I$ is the inertia tensor of the sphere, and $\omega_s$ is the spin rate of the sphere.

With a spin rate of 4 Hz and an approximate nutation angle of about 3 degrees, the diameter of the nutation cone is approximately 5/8$^{th}$ of an inch. For that much "wobble" in the sphere, the outer edges of the deck plate will move approximately 0.210 inches. The acceleration due to this motion must be accounted for, as discussed in §DYNAMICS.G: Accelerometer Response, as well as results shown in §FLIGHT DATA & TEST RESULTS.C: Flight Nutation & Precession. The precession frequency is close to one Hertz.

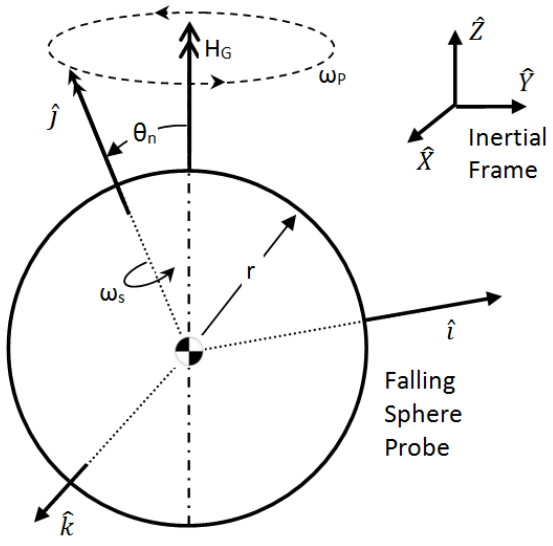


**Figure 20: Falling Sphere Probe in Torque-free Motion**

# VIBE CALIBRATION

A vibe shake test was used to characterize the science accelerometers. From this data the calibration curve for these accelerometers is determined. This calibration curve gives the correction factors to the manufacturer supplied sensor specifications, or the general calibration performed by the manufacturer.

The test consisted of gently shaking the system in each of the three principles axes of the Sphere Centered Fixed (SCF) coordinate system. A sufficiently thick fixture, so as to not affect any of the sphere's mode shapes or frequencies, was used to attach the sphere to the vibrating table. The setup for the vibration testing is shown in Figure 21. The shaker table has an accelerometer on it acting as the control response to the system; the load seen on the table is not constant as seen in Figure 22. The result for sphere 41.091 for the 400 mg shake is shown in Figure 23. The data recorded by the Falling Sphere has roll-off due to the filtering of the electronics board. The frequency range of most interest, and expected to see on flight, is the range from 0.2 Hz to 20 Hz. This frequency range is affect least of all by the filtering. This roll-off is evident in the calibration curve of Figure 23, the curve is not linear for all the data. It is however, fairly linear in the range of interest.

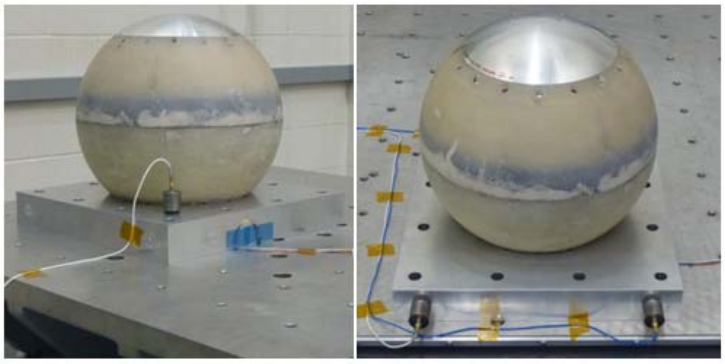

**Figure 21: Vibration Setup for Accelerometer Calibration**

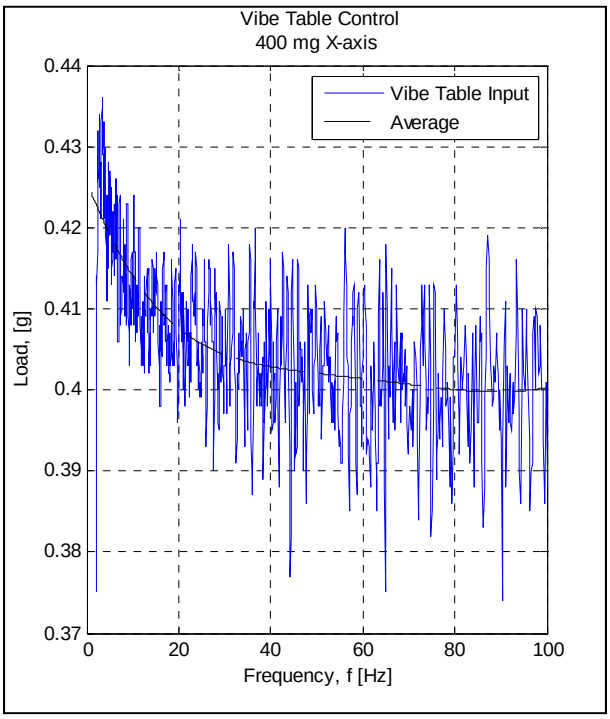


**Figure 22: Vibration Input for Accelerometer Calibration**

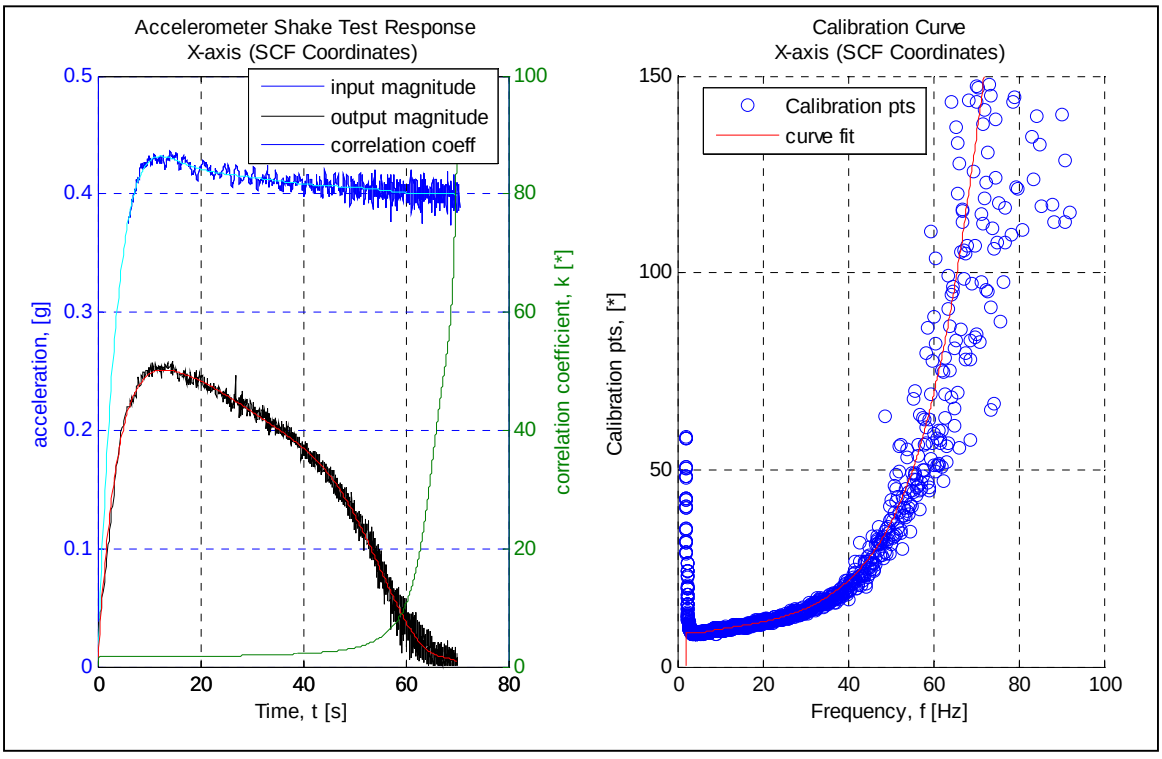


**Figure 23: Calibration curve for Accelerometer (sphere 41.091, Channel 1)**

# GYRO CALIBRATION

A gyro spin test was conducted to calibrate the gyro sensors in the µIMU device. From this test a calibration curve is determined. Similarly, this calibration curve gives the correction factors to the manufacturer supplied sensor specifications.

The test consisted of spinning the sphere about each of its axes on a precision spin table at the Wallops Flight Facility for seven different rotation rates for both clockwise and counter-clockwise rotations, giving fifteen steps total including no spin rate (0 deg/s). Each rotation rate was held for a minimum of ten seconds, giving over 1,000 samples per step in rotation rate. Note that the sphere's coordinate system in NOT the same as the coordinate system of the µIMU device. This coordinate system difference is shown in Figure 24. The results from the test are first rotated to the Sphere Centered Fixed (SCF) coordinate system and then processed to determine the calibration.

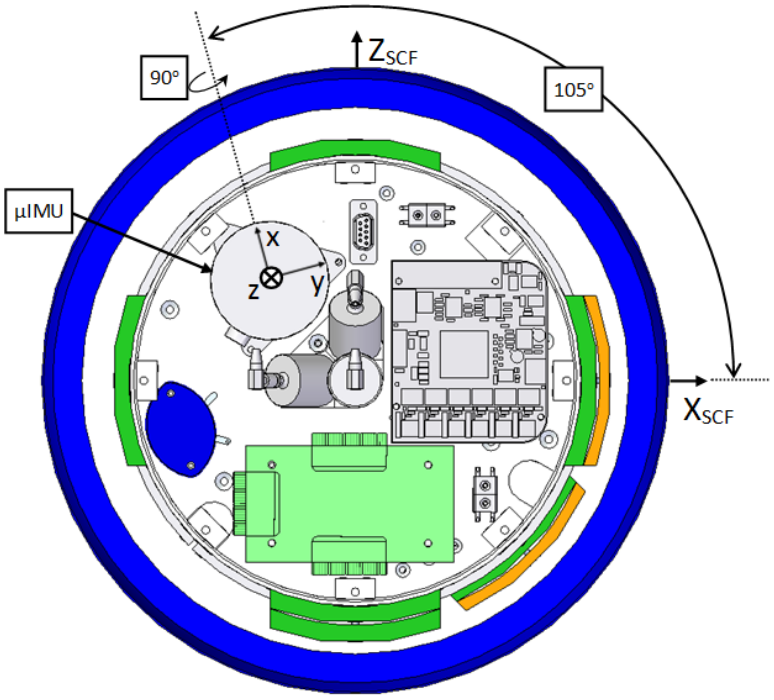


**Figure 24: Coordinate System rotation for µIMU**

The calibration results for sphere 41.091 are shown below in Figure 25. As can be seen in the data from the test, the y-axis gyro (along the sphere spin axis) has a higher range than the gyros in the x and z axes. The saturation limit on the spin axis gyro is about 2000 deg/s, whereas the other two gyros saturation limits are about 200 deg/s. This is evident in the calibration curve, where the data turns from a linear relationship to a non-linear one.

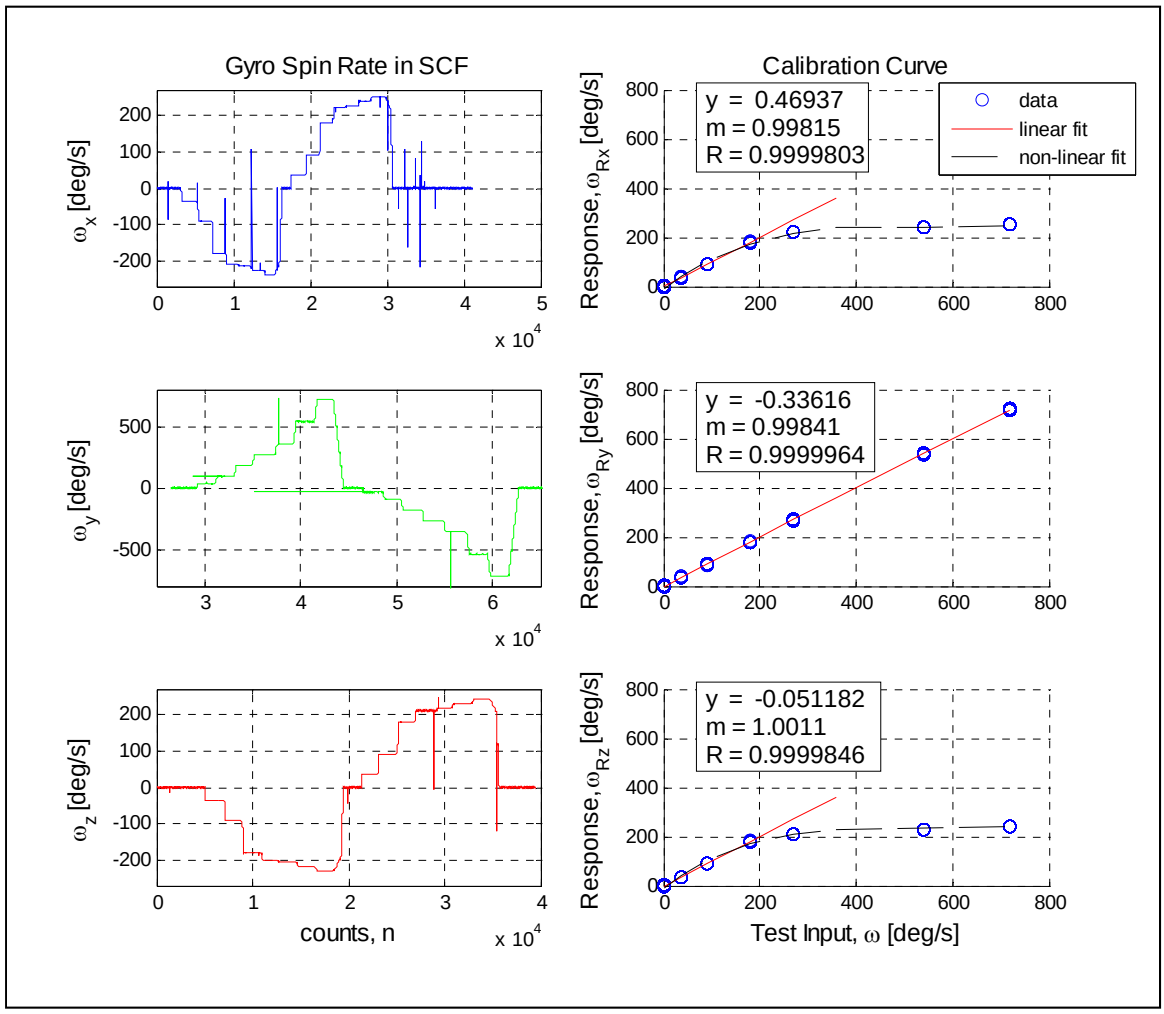


**Figure 25: Calibration Curve for Gyro Calibration (sphere 41.091)**

## PREDICTED EJECTION CONDITION & TIMELINE

The launch vehicle analysis and Flight performance was completed by NSROC II at Wallops Flight Facility (WFF). The Falling Sphere Probe was a secondary payload onboard a Terrier Mk70-Improved Orion, launched out of WFF, Virginia. At the time of ejection, the predicted position and velocity are shown in Table 3.

**Table 3: WFF Predicted Conditions at Time of Ejection**

| Event | Time [s] | Altitude [km] | Range [km] | Velocity [m/s] | Mach No. | Q [psf] | Flight Elevation [deg] |
|---|---|---|---|---|---|---|---|
| Sphere Ejection | 70.0 | 82.2 | 26.7 | 1314.2 | 4.8 | 0.3 | 68.2 |

# FLIGHT DATA & TEST RESULTS

The data collected from the sensors during flight was done in semi-real time. All data was downloaded and saved during the flight, the sphere was not recovered. It shall spend the rest of its days at the bottom of the Atlantic Ocean off the coast of Virginia. The launch took place on July 10, 2011 at 14.00.15 Universal Time (UTC) at Wallops Flight Facility. The Falling Sphere Probe was a secondary payload with another neutral wind measuring campaign, a lithium chemical release method. The primary payload, the science payload, was onboard another rocket. Both rockets (science payload and neutral wind measuring payload) were to be launched within 90 seconds of each other. Two flights of these sets or pairs of rockets were scheduled. The first in an active condition, the second to be launched into a quiet environment, approximately a 2 day turn around. However, there was a malfunction with the chemical release testing and that method failed completely and as a result, the second launch set was scrubbed. With that, the Falling Sphere Probe #41.091 was the only instrument system to gather wind data from the first launch set.

A Javad TR-G2 GPS was onboard the sphere for position tracking. The communication link consisted of Wallops' *Mosquito* PCM stack, a transmitter, and standard wrap around antenna (as shown in Figure 3 and Figure 5). There was a loss of signal (LOS) from the GPS approximately between the times $t = 10$ seconds to $t = 30$ seconds. This is likely due to the intensity of the launch and the high g-loads experienced. The Terrier Mk70 burnout was at $t = 6.2$ seconds, and the Improved Orion ($2^{nd}$ stage) ignition was at $t = 15.0$ seconds. The telemetry signal was not lost during launch and had a signal lock for the entire flight.

Throughout the burn of both stages the Positional Dilution of Precision (PDOP) of the GPS was anywhere from good to fair. The rating values being:1-2 as *Excellent*, 2-5 as *Good*, 5-10 as *Moderate*, and 10-20 as *Fair*. After the nose cone ejection, the PDOP was *Good* to *Excellent* for the rest of the flight. The average PDOP value was approximately 2.1 for the entire free flight of the sphere. The PDOP for the GPS signal is shown in Figure 26;the LOS is also evident in the figure.

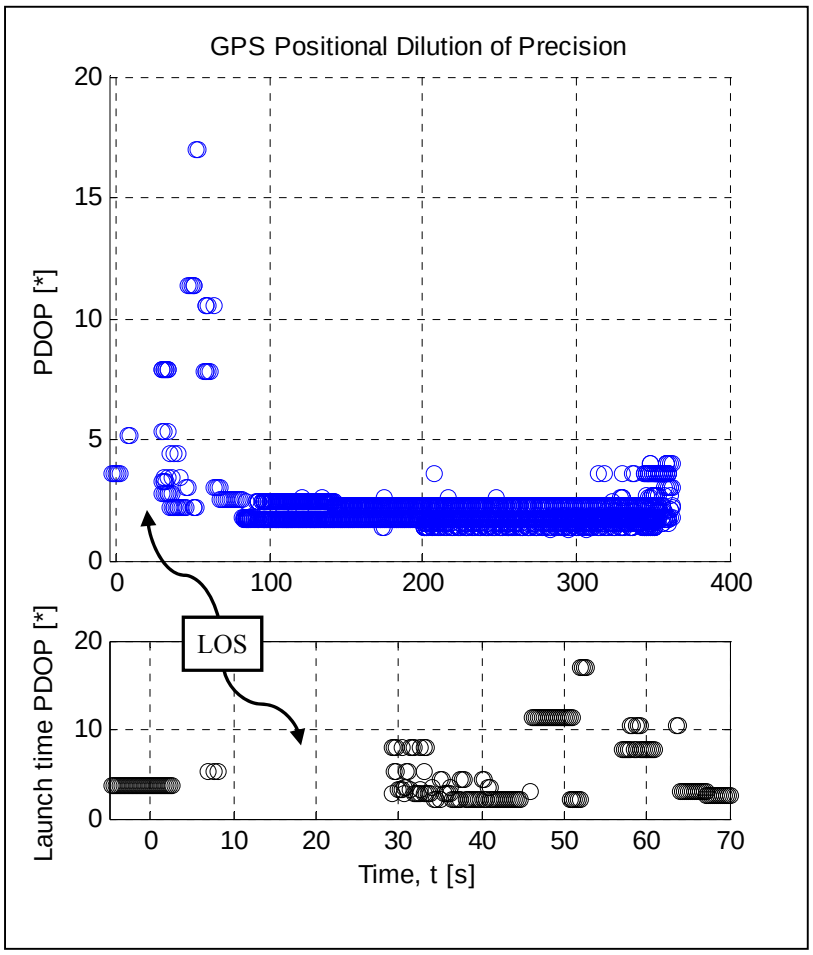


**Figure 26: GPS Positional Dilution of Precision**

## A. Simulation vs. Real Data

The first look at the data was to compare what was actually collected to what was expected based on the math model. The dynamic response was close to the predicted, calculated flight trajectory. There are many real world affects that are hard to account for and predict precisely. Since no wind tunnel testing was performed, many flow parameters were estimated, such as drag coefficients. The atmosphere model used in the simulation to predict the atmospheric temperature and air density is the 2001 United States Naval Research Laboratory Mass Spectrometer and Incoherent Scatter Radar Exosphere. This model calculates the neutral atmosphere empirical model from the surface to lower exosphere (0 m to 1,000,000 m).

The GPS collected data is compared to the model prediction, and the altitude and velocity of the sphere is seen in Figure 27 and Figure 28below.

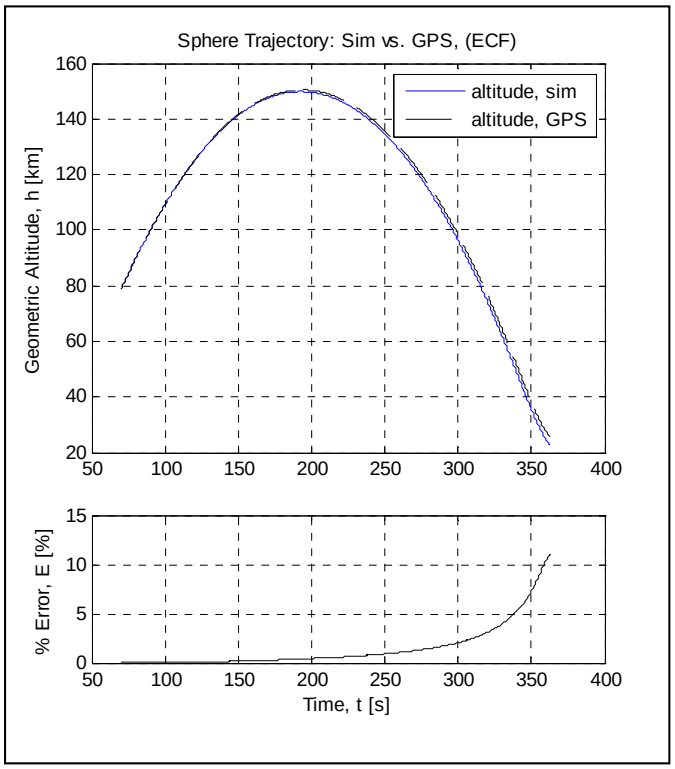


**Figure 27: Simulation vs. GPS results, Altitude [km]**

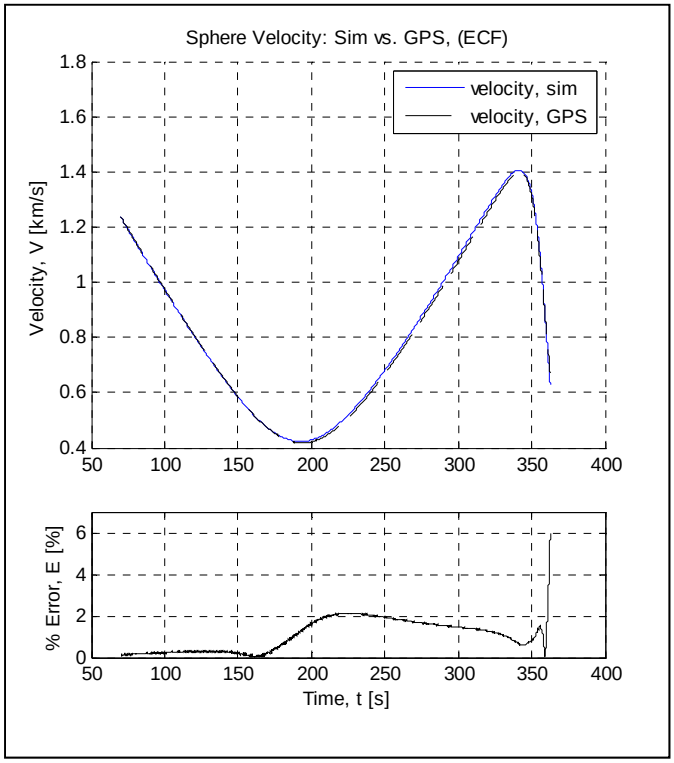


**Figure 28: Simulation vs. GPS results, Velocity [km/s]**

The high velocity of the sphere is more evident when looking at the Mach number. As seen in Figure 29, the sphere is traveling at a Mach number close to 4.5 when ejected. For the duration of the flight, the sphere is traveling primarily at supersonic speeds, with transonic flight occurring at apogee. The sphere did not have the capability of measuring the outside temperature during flight; therefore, the speed of sound through the medium (air) was calculated from the model and used in the calculation of the Mach number for the GPS comparison.

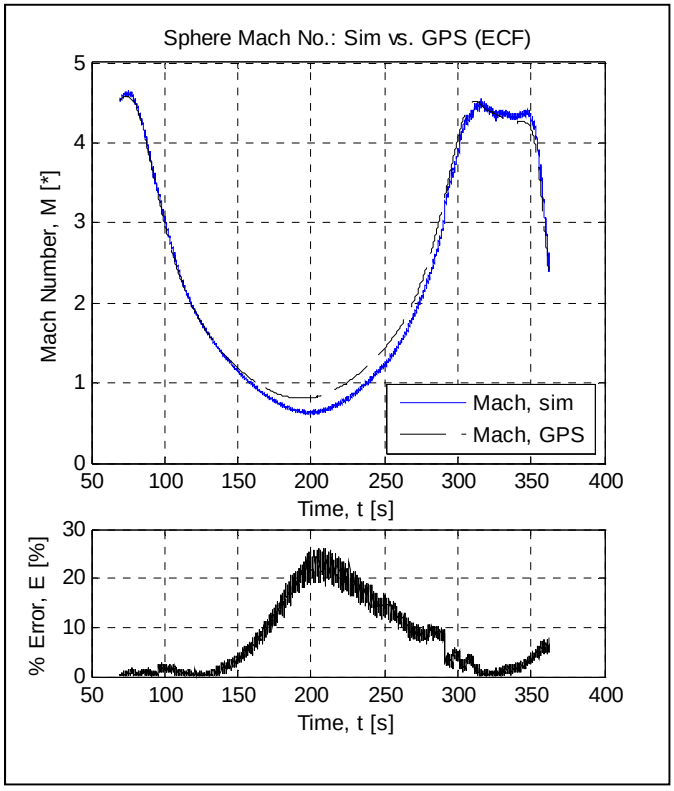


**Figure 29: Simulation vs. GPS results, Mach No. [*]**

## B. Science Accelerometers

The FSP science accelerometer requirements were that the sphere needed the capability of measuring in the acceleration range of 200 ng to 20 μg, with a 10 ng resolution. (The requirements come from a study performed by Clemson University). With the given requirements, the design requirements were set to measuring the acceleration range of 100 ng to 100 μg. The raw accelerometer range is ± 1 μg to ± 0.25 g, with a 0.1 μg resolution (see Appendix A, for accelerometer spec sheet). The absolute resolution of the system was defined by the analog to digital converter (ADC). With a range of 0.5 g on the accelerometer, and sampling $2^{27}$ bits, the converter's resolution is 3.725 ng/bit, which is approximately 0.1 μg. This resolution was verified with testing. The sampling rate of the accelerometers was approximately 4 kHz, with a 20 Hz filter. The filter was to eliminate noise on the signal outside the frequency range of interest. The initial design was for a spin rate of the sphere at 2 Hz. With that, the filter was set a decade above and

a decade below the target spin rate. The filter range was set as 0.2 Hz to 20 Hz. The over sampling allows post-processing to reach ± 100 ng with a 0.1 μg resolution.

The MEMSense μIMU device was used primarily for determining the sphere's precession rate with cone angle, and the spin rate about each axis. The science accelerometers were intended to track the neutral wind measurements. The measuring technique was to use six ultra-precision accelerometers in a configuration discussed and shown in §OVERALL DESIGN.A: Sensors. Each accelerometer is paired with another one pointing in the opposite direction and is AC coupled. Because they are AC coupled, during accelerometer saturation the signal output is zero (hard saturation, see Figure 31).

The science accelerometer signal was saturated in flight and the data from these instruments, as a result, is not as good as was expected. Any neutral wind measurements taken were lost during saturation of these accelerometer measurements. The cause of saturation is believed to be due to excessive coning caused by not having a clean ejection of the FSP from the rocket. In addition to coning, the spin rate was much higher than anticipated and may also be a source of saturation on the science accelerometer signal. The spin rate was, on average, about 6.6 Hz, whereas the design spin rate was ≤ 4 Hz. The measured spin rates of the sphere are shown in Figure 30. The ADC board has a lower saturation limit than the science accelerometers, about 0.23 g's, and when the signal is not saturated, any neutral wind measurements is masked by the excessive coning. Any neutral wind measurement data collected is deemed questionable.

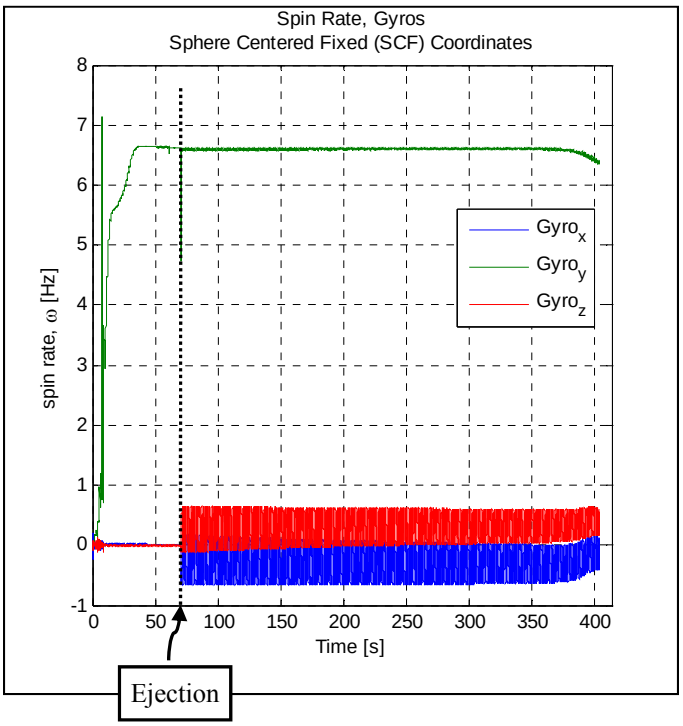


**Figure 30: Measured Spin Rate [Hz] of Sphere (µIMU)**

There were two kinds of saturations that occurred in flight. One is a hard saturation where the ADC and the science accelerometers go into saturation. The time constant for coming out of saturation was not characterized before the flight, but from the data it appears to be approximately 22 seconds. The second kind is a soft saturation, where the ADC is in saturation but not necessarily the accelerometers. Both the hard and soft saturation is seen in Figure 31 below. Further study is needed to verify the cause of saturation and how to best analyze and interpret the data.

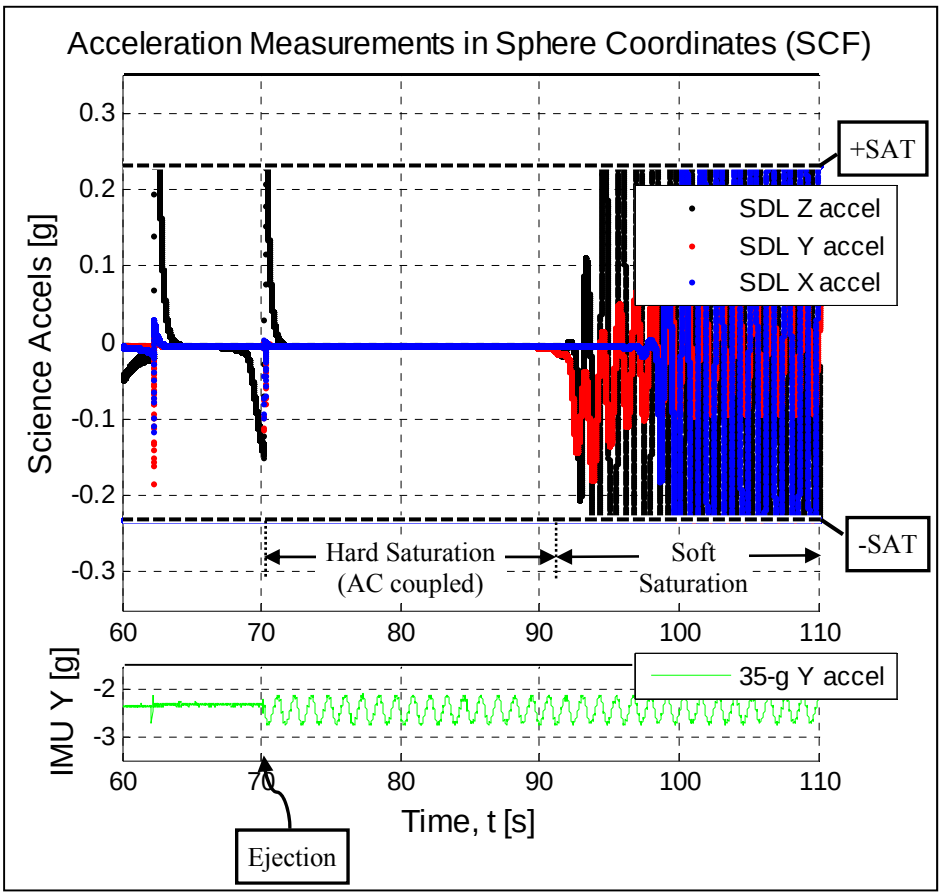


**Figure 31: Science Accelerometer signal: Hard Saturation & Soft Saturation (IMU Y axis ≡ Spin Axis)**

### C. Flight Nutation & Precession

A look into the gyro flight data will give some insight into the "wobble" of the sphere in flight. The nutation angle is calculated as described above in §BALANCING.B.3: Falling Sphere Probe Angle of Precession. The nutation angle varies from 0.46 degrees to 7.10 degrees. This is shown in Figure 32. The precession rate is also shown with a minimum rate at 0.54 Hz to a maximum of 0.76 Hz, see Figure 33.

Since the sphere is not perfectly balanced the centripetal accelerations caused from the wobble in the sphere and the spin on the sphere are calculated using the equation, $a=-\omega^2 r$ .For worst case scenarios, the accelerations the sphere sees from the wobble is 0.09 g's and the acceleration the sphere sees from its spin rate is 3.31 g's. Clearly at this level of g's the instrumentation is saturated (recall that the accelerometers

range is 0.5 g peak – see Appendix 0). The total combined acceleration seen is 3.40 g's (this takes into account the angular offset or mounting angle of approx. 45 degrees of the accelerometer).

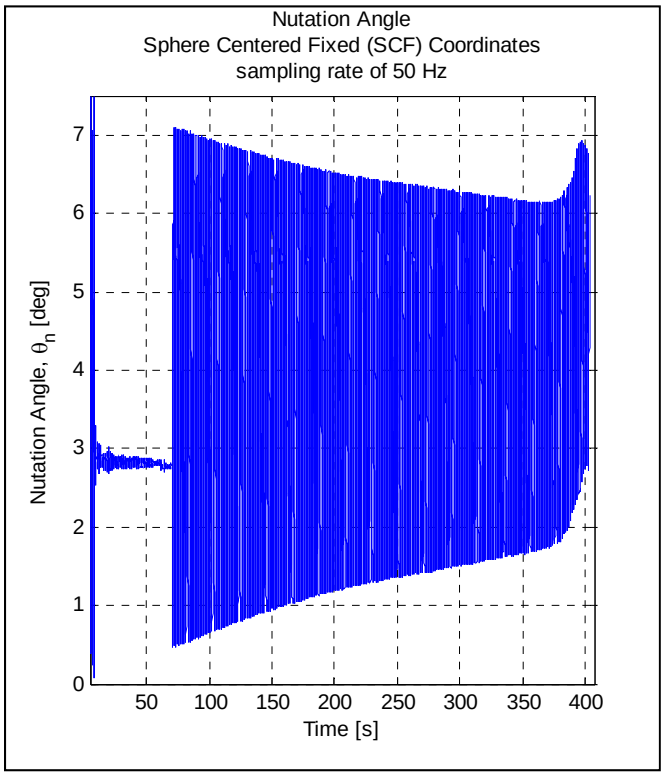


**Figure 32: Flight Nutation Angle, Sphere 40.091**

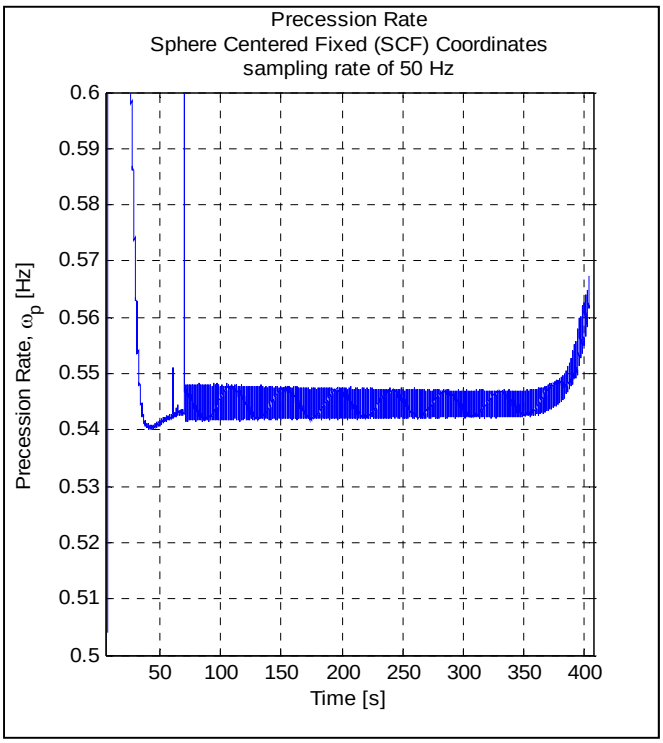


**Figure 33: Flight Precession Rate, Sphere 40.091**

Assuming that the balance of the sphere was to remain the same, in order to not go into saturation, the spin rate of the sphere would have to be 1.54Hz or less. (For calculating the centripetal acceleration due to the wobble, $r_{horz}$ was used for $r$. In calculating the centripetal acceleration due to the sphere's spin rate, $h_{vert}$ was used for $r$. Refer to section § DYNAMICS.G: Accelerometer Response, for definition of distances).

## D. Further Processing of Flight Data

An Extended Kalman filter is used to process the data measurements to estimate the attitude of a spacecraft during flight or post flight. The quaternion is used to represent the attitude because it has no singularities and the kinematics equation is bilinear. The filter will process magnetometer data and Inertial Measurement Unit (IMU) data using a discrete time method. Both the magnetometer and the IMU have the same sample rate of 50 Hz, so there is a measurement from each at every time step. For the full filter derivation of equations and process see ref [8]. A summary of the filter steps and equation can be found in Table 4.

**Table 4: Discrete Extended Kalman Filter for Attitude Estimation**

| | |
|---|---|
| Initialize | $\hat{q}(t_0) = \hat{q}_0, \quad \beta(t_0) = \beta_0, \quad \boldsymbol{P}(t_0) = \boldsymbol{P}_0$ |
| Gain | $K = P_k^- H_k^T {P_{residual}}^{-1}, \quad P_{residual} = [H_k P_k^- H_k^T + R]$<br>$H_k(\hat{x}_k^-) = \begin{bmatrix} [A(\hat{q}^-)r_1 \times] & 0_{3x3} \\ \vdots & \vdots \\ [A(\hat{q}^-)r_n \times] & 0_{3x3} \end{bmatrix}$ |
| Update | $P_k^+ = [I_{6x6} - K_k H_k] P_k^- [I_{6x6} - K_k H_k]^T + K_k R K_k^T$ (Joseph Form)<br>$\Delta\hat{\tilde{x}}_k^+ = K[\tilde{y}_k - h_k], \quad \text{residual}, \epsilon = [\tilde{y}_k - h_k]$<br>$\Delta\hat{\tilde{x}}_k^+ = \left[\delta\hat{\alpha}_k^{+T} \;\; \Delta\hat{\beta}_k^{+T}\right]^T$<br>$h_k = \begin{bmatrix} A(\hat{q}^-)r_1 \\ \vdots \\ A(\hat{q}^-)r_n \end{bmatrix}$<br>$\hat{q}_k^+ = \hat{q}_k^- + \frac{1}{2}\Xi(\hat{q}_k^-)\delta\hat{\alpha}_k^+$<br>$\hat{q} = \hat{q} \Big/ \sqrt{\hat{q}^T\hat{q}}$ (Normalize the Quaternion)<br>$\Xi(q) \equiv \begin{bmatrix} q_4 I_{3x3} + [\varrho \times] \\ -\varrho^T \end{bmatrix}, \quad \varrho = [q_1 q_2 q_3]^T$<br>$\hat{\beta}_k^+ = \hat{\beta}_k^- + \Delta\hat{\beta}_k^+$ |
| Propagation | $\widehat{\omega}_k^+ = \tilde{\omega}_k - \hat{\beta}_k^+$<br>$\hat{\beta}_{k+1}^- = \hat{\beta}_k^+$<br>$\hat{q}_{k+1}^- = \bar{\Omega}(\widehat{\omega}_k^+)\hat{q}_k^+$<br>$\bar{\Omega}(\widehat{\omega}_k^+) \equiv \begin{bmatrix} \cos\left(\frac{1}{2}\|\widehat{\omega}_k^+\|\Delta t\right) I_{3x3} - [\hat{\psi}_k^+ \times] & \hat{\psi}_k^+ \\ -\hat{\psi}_k^{+T} & \cos\left(\frac{1}{2}\|\widehat{\omega}_k^+\|\Delta t\right) \end{bmatrix}$<br>$\hat{\psi}_k^+ \equiv \frac{\sin\left(\frac{1}{2}\|\widehat{\omega}_k^+\|\Delta t\right)\widehat{\omega}_k^+}{\|\widehat{\omega}_k^+\|}$<br>$P_{k+1}^- = \Phi_k P_k^+ \Phi_k^T + G_k Q_k G_k^T, \quad G_k = \begin{bmatrix} -I_{3x3} & 0_{3x3} \\ 0_{3x3} & I_{3x3} \end{bmatrix}$ |

$$Q_k = \begin{bmatrix} \left(\sigma_v^2 \Delta t + \frac{1}{3}\sigma_u^2 \Delta t^3\right) I_{3x3} & -\left(\frac{1}{2}\sigma_u^2 \Delta t^2\right) I_{3x3} \\ -\left(\frac{1}{2}\sigma_u^2 \Delta t^2\right) I_{3x3} & (\sigma_u^2 \Delta t) I_{3x3} \end{bmatrix}$$

$$\Phi = \begin{bmatrix} \Phi_{11} & \Phi_{12} \\ \Phi_{21} & \Phi_{22} \end{bmatrix}$$

$$\Phi_{11} = I_{3x3} - [\hat{\omega} \times] \frac{\sin\left(\frac{1}{2}\|\hat{\omega}\|\Delta t\right)}{\|\hat{\omega}\|} + [\hat{\omega} \times]^2 \frac{\{1 - \cos(\|\hat{\omega}\|\Delta t)\}}{\|\hat{\omega}\|^2}$$

$$\Phi_{12} = [\hat{\omega} \times] \frac{\{1 - \cos(\|\hat{\omega}\|\Delta t)\}}{\|\hat{\omega}\|^2} - I_{3x3}\Delta t - [\hat{\omega} \times]^2 \frac{\{\|\hat{\omega}\|\Delta t - \sin(\|\hat{\omega}\|\Delta t)\}}{\|\hat{\omega}\|^3}$$

$$\Phi_{21} = \mathbf{0}_{3x3}$$

$$\Phi_{22} = I_{3x3}$$

where$[\vec{x} \times]$ is the cross product matrix, defined in Eq. (4.1.6)

The filter is first initialized to a known state variable and error-covariance matrix. The filter state is the attitude angle error and the gyro bias. The attitude equations are linearized and the quaternion scalar part is approximately one, that is,$q_4 \approx 1$. Therefore, the state vector is reduced by one state and goes from a 7x1 to a 6x1. The error-covariance matrix is comprised of the variances on the attitude in the 1st three diagonal terms, and the gyro error variance in the last three diagonal terms.

The initial quaternion is found from the known orientation of the launch vehicle on the launch pad. From the known initial position, a rotation matrix from Inertial to Body (sphere) coordinates can be determined. The rotation sequence will go from Earth Centered Inertial (ECI) to North East Down (NED) and then from NED to Body coordinates. Given the Azimuth, elevation, and rail orientation of the launch vehicle's initial position, the orthogonal rotation matrix from ECI to Body is expressed as,

$$\boldsymbol{R}_{ECI}^{B} = \boldsymbol{R}_{NED}^{B} \boldsymbol{R}_{ECI}^{NED} = \begin{bmatrix} \hat{\imath}_x^T \\ \hat{\imath}_y^T \\ \hat{\imath}_z^T \end{bmatrix} \begin{bmatrix} \hat{\imath}_N^T & \hat{\imath}_E^T & \hat{\imath}_D^T \end{bmatrix} \tag{10.4.1}$$

Which are essentially two rotations from a NED frame to a reference frame. From Body to NED, the unit vectors are

$$\hat{\imath}_x = \frac{UP \times R_{By}}{\left\| UP \times R_{By} \right\|} \tag{10.4.2}$$

$$\hat{\imath}_y = \frac{-R_{By}}{\left\| R_{By} \right\|} \tag{10.4.3}$$

$$\hat{\imath}_z = \hat{\imath}_x^T \times \hat{\imath}_y^T \tag{10.4.4}$$

where $UP$is a unit vector in the "up" direction, or in the negative NED "down" vector. The vector $R_{By}$is a vector in the direction of the spin axis of the sphere. This is simply the spherical coordinates to the origin of the Body coordinate axes represented in Cartesian coordinates. The elements of the spherical coordinates are the given Azimuth, elevation and range. This is clearly seen in Figure 34. The orientation of the sphere in the rocket with respect to the rail is the positive z-axis points towards the launch rail.

The familiar unit vectors in NED are,

$$\hat{\imath}_N = \hat{\imath}_E^T \times \hat{\imath}_D^T \tag{10.4.5}$$

$$\hat{\imath}_E = \frac{\omega_E \times R_{sc}}{\| \omega_E \times R_{sc} \|} \tag{10.4.6}$$

$$\hat{\imath}_D = \frac{-R_{sc}}{\| R_{sc} \|} \tag{10.4.7}$$

where$R$ is the position vector from the center of the earth to the cg of the spacecraft, and $\omega_E$ is the rotation rate vector of the earth in rad/s.

With a given DCM from ECI to Body, the initial quaternion can be calculated as [14],

$$q_4 = \pm 0.5\sqrt{1 + A_{11} + A_{22} + A_{33}} \tag{10.4.8}$$

$$q_1 = 0.25(A_{23} - A_{32})/q_4 \tag{10.4.9}$$

$$q_2 = 0.25(A_{31} - A_{13})/q_4 \tag{10.4.10}$$

$$q_3 = 0.25(A_{12} - A_{21})/q_4 \tag{10.4.11}$$

where *A* is the DCM calculated in Eq. (10.4.1), and $q_4$ is the scalar part of the quaternion and $q_1$, $q_2$, and $q_3$ is its vector part.

The initial bias input to the filter comes from the gyro calibration data. The bias is taken as the average on the 0 deg/s input on each of the 3 axes. From the gyro calibration data, the initial bias is (in SCF coordinates),

$$\beta_0 = [0.330, -0.210, -0.148]^T \ (deg/s) \tag{10.4.12}$$

From this data, the standard deviation is calculated across the sample and the variance is determined as the square of the standard deviation. The covariance on the gyro is (in SCF coordinates),

$$\boldsymbol{P}_{gyro} = \begin{bmatrix} \sigma_{g,x}^2 & 0 & 0 \\ 0 & \sigma_{g,y}^2 & 0 \\ 0 & 0 & \sigma_{g,z}^2 \end{bmatrix} = \begin{bmatrix} 0.377^2 & 0 & 0 \\ 0 & 0.637^2 & 0 \\ 0 & 0 & 0.334^2 \end{bmatrix} (deg/s)^2 \tag{10.4.13}$$

The initial error-covariance matrix is the combination of the attitude covariance matrix and the gyro covariance matrix. The attitude covariance matrix is taken from the launch conditions. It is assumed that the initial position of the launch vehicle is known to within ±15 degrees. Then the attitude covariance and

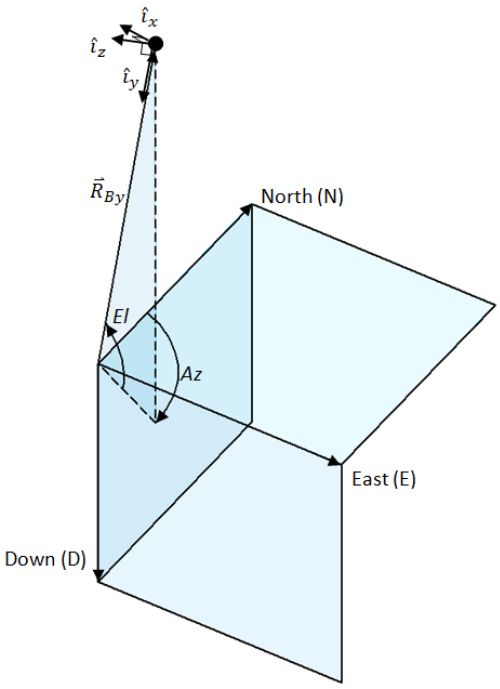


**Figure 34: Azimuth, Elevation & Range to NED**

initial error-covariance matrix are,

$$\boldsymbol{P}_{attitude} = \begin{bmatrix} \sigma_{a,x}^2 & 0 & 0 \\ 0 & \sigma_{a,y}^2 & 0 \\ 0 & 0 & \sigma_{a,z}^2 \end{bmatrix} = \begin{bmatrix} 15^2 & 0 & 0 \\ 0 & 15^2 & 0 \\ 0 & 0 & 15^2 \end{bmatrix} (deg)^2 \tag{10.4.14}$$

$$\boldsymbol{P}_0 = \begin{bmatrix} \boldsymbol{P}_{attitude\ (3x3)} & \boldsymbol{0}_{(3x3)} \\ \boldsymbol{0}_{(3x3)} & \boldsymbol{P}_{gyro\ (3x3)} \end{bmatrix} \tag{10.4.15}$$

To improve the performance of the filter a batch method, also known as a *smoother*, is used to "smooth" out the effects of measurement noise. The disadvantage to using a smoother is they cannot be used in real-time, which in this case is not a problem since all the data processing is done post flight. The advantage, however, is in providing the state estimates with a lower error-covariance than sequential methods. The batch method used in this model is a *Fixed-Interval Smoothing* type. This type uses the entire batch of measurements within an interval to estimate the states within in the interval. Smoothers use measurements made before and after a certain time *t*. The smoother uses two filters: a forward-time filter and a backward-time filter. This is seen in the illustration below in Figure 35for a fixed interval. The most common fixed-interval smoother, the Rauch, Tung, and Striebel (RTS) smoother will be used. This smoother combines the backward filter and smoother into one single backward recursion[8].

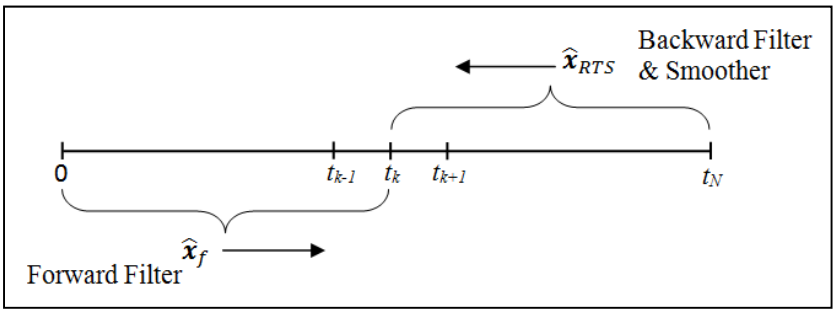


**Figure 35: Forward and Backward Filtering & Smoothing**

The full derivation of the RTS Smoother is given in [8], a summary of the smoother is given in Table 5. The Forward Kalman Filter is executed using the equations and steps outlined in Table 4 above. The propagated and updated states and covariance from the forward filter are used to compute the gain and

covariance of the smoother. The smoother estimate equation is executed backward in time. (Subscript *f* indicates a forward-time filter, and subscript *b* indicates a backward-time filter).

**Table 5: Discrete-Time RTS Smoother**

| | |
|---|---|
| Model | $x_{k+1} = \Phi_k x_k + \Gamma_k u_k + G_k w_k, \qquad w_k \sim N(0, Q_k)$<br>$\hat{y}_k = \mathrm{H}_k x_k + v_k, \qquad v_k \sim N(0, R_k)$ |
| Forward Filter | Execute Forward Filter, See Table 4 |
| Smoother Initialize | $\hat{x}_{b\,N} = \hat{x}^+_{f\,N}, \qquad P_{b\,N} = P^+_{f\,N}$ |
| Gain | $\mathrm{K}_{b\,k} = P^+_{f\,k}\Phi^T_k\left(P^-_{f\,k+1}\right)^{-1}$ |
| Covariance | $P_{b\,k} = P^+_{f\,k} - \mathrm{K}_{b\,k}\left[P^-_{f\,k+1} - P_{b\,k+1}\right]\mathrm{K}^T_{b\,k}$ |
| Estimate | $\hat{x}_{b\,k} = \hat{x}^+_{f\,k} + \mathrm{K}_{b\,k}\left[\hat{x}_{b\,k+1} - \hat{x}^-_{f\,k+1}\right]$ |

To verify if the Extended Kalman Filter is running correctly, simulated data can be created from the dynamic prediction model (using the governing equations of motion, Eq. (4.1.3) and Eq. (4.1.4)). The magnetic field and all inputs need to be known. All inputs or specs to the would-be-sensors can come directly from either the MEMSense spec sheet or the calibration data, i.e. noise levels, sample frequency, etc…

The results from a simulation were interesting. As seen in Figure 36, the Extended Kalman filter is not keeping up with the dynamics of the simulation. The error shown is much too high. The sampling rate is too small (50 Hz) for the spin of the spacecraft, which is spinning at approximately 6.6 Hz. At that spin rate, the sphere is rotating at 2376 deg/s (degrees per second)! Yet with a sampling rate of 50 Hz ($\Delta t = 0.02$ s), it is only capturing data at every 47.52 degrees. That kind of resolution does not provide any useful attitude information. Generally, in order to capture the dynamics adequately it is desired to sample every 0.1 degrees or less, with a maximum at 1.0 degrees. Even at capturing at a desired maximum resolution (1.0 degrees), the sampling frequency of the µIMU (magnetometer & gyros) would need to be 2376 Hz, or

approx. 2.4 kHz. For a resolution to 0.1 degrees, the μIMU sampling frequency would need to be approx. 24 kHz! A more realistic sampling rate of 4.8 kHz would give a 0.5 degree resolution. Even at that, the μIMU sampling rate is nowhere near the required rate. For comparison, at 4.8 kHz sampling rate the attitude can be estimated much more accurately as shown in Figure 37.

With only a magnetometer sensor on board and average gyros, the attitude is not determined at this sampling rate with this filter design. This is a time varying system and a magnetometer is NOT observable at an instant in time. However, for a finite length of time and with a changing magnetic field, the system can be observable.

(The following data will be shown for illustrative purposes for the case of a sampling rate of 4.8 kHz, it is also representative of the data ran at 50 Hz. It is only run for 20 seconds of data). A quick look at the angular momentum will indicate if the simulation is working as it should. For a properly working simulation and filter estimation, the angular momentum should remain constant. With real data (or simulated "real" data) this should be fairly constant and is evident in Figure 38. As another check, the residuals should look like a zero mean Gaussian random white noise signal; this is seen in Figure 39.

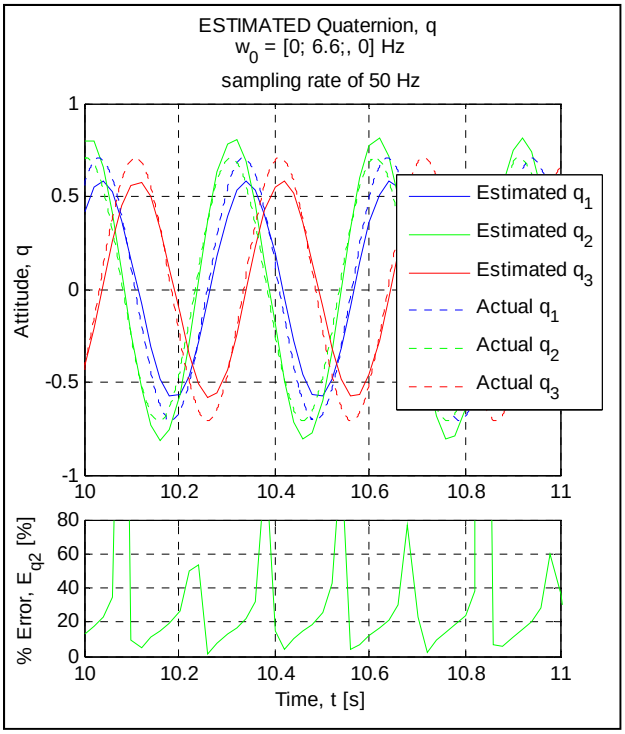


**Figure 36: EKF Estimated Quaternion @ 50 Hz sampling rate**

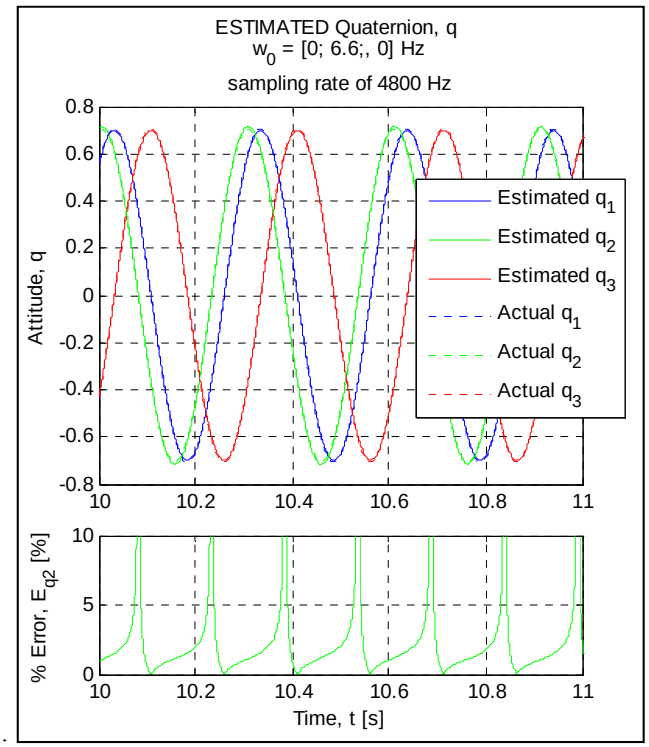


**Figure 37: EKF Estimated Quaternion @ 4800 Hz sampling rate**

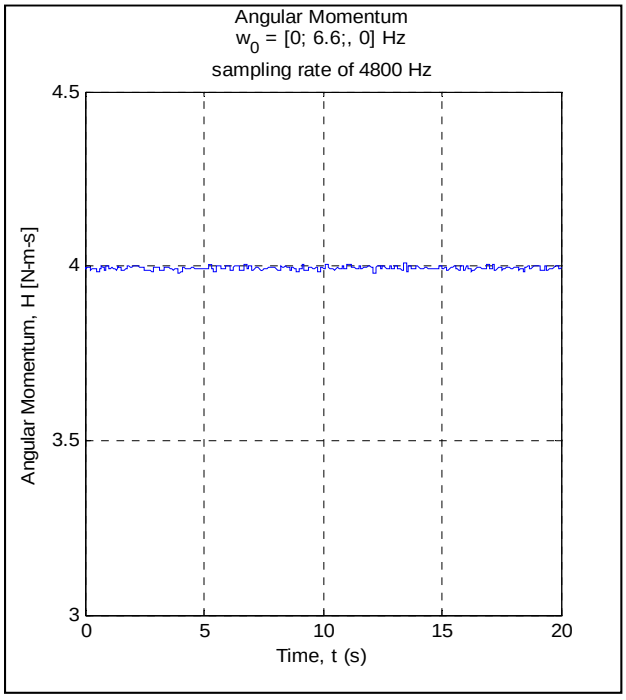


**Figure 38: EKF Angular Momentum of Simulated Data**

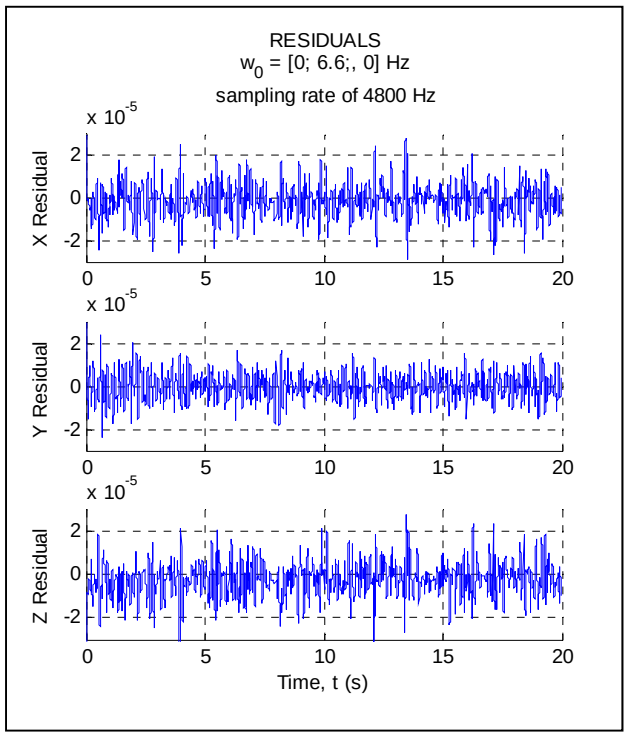


**Figure 39: EKF Residuals of Simulated Data**

The estimated rotation angles of the sphere to ECI coordinates are shown in Figure 40. It is clear that the yaw angle is the rotation angle (rotation ± 180$^o$). The error of the rotation angles are shown in Figure 41. It is apparent that the filter had trouble tracking the yaw angle, $\psi$, which is about the spin axis. The yaw angle rotates through a ± 180 degrees. As it approaches a roll-over, going from +180 deg to -180 deg, any deviation between the actual angle of rotation and the estimated angle will result in an extreme error. This is seen by the large data spikes in the yaw angle error (Figure 41).

The Bias estimation and angular velocity estimation are shown in Figure 42 and Figure 43respectively. It is evident that the filter is converging to a solution within a relatively short time frame (less than 1 minute).

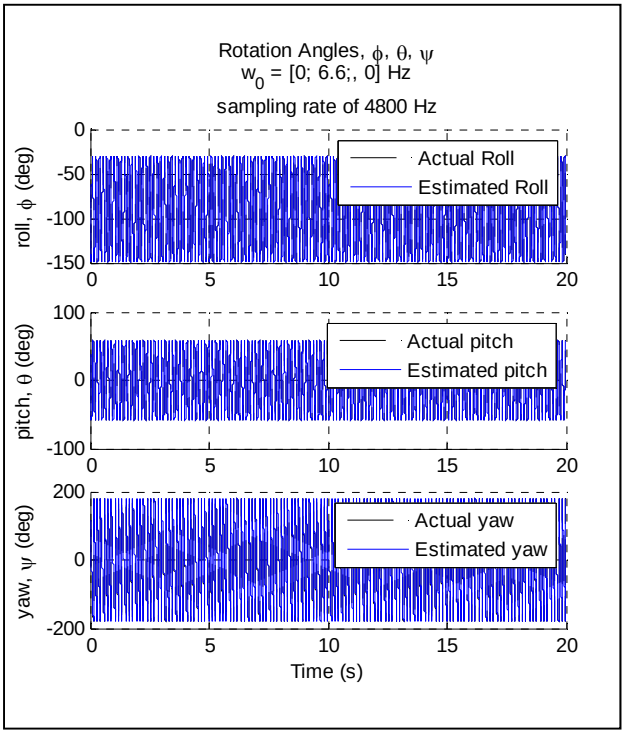


**Figure 40: EKF Euler Rotation Angles: Roll, Pitch, Yaw of Simulated Data**

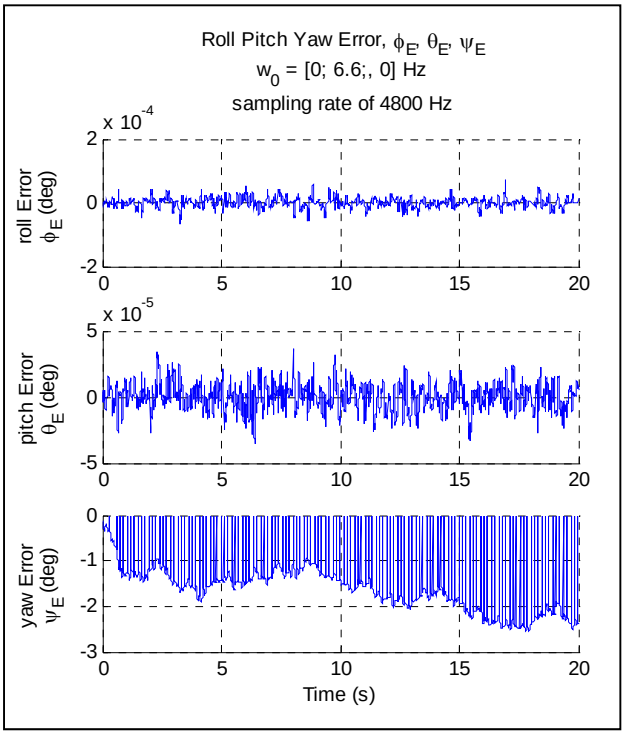


**Figure 41: EKF Roll, Pitch, & Yaw Estimation Errors on Simulated Data**

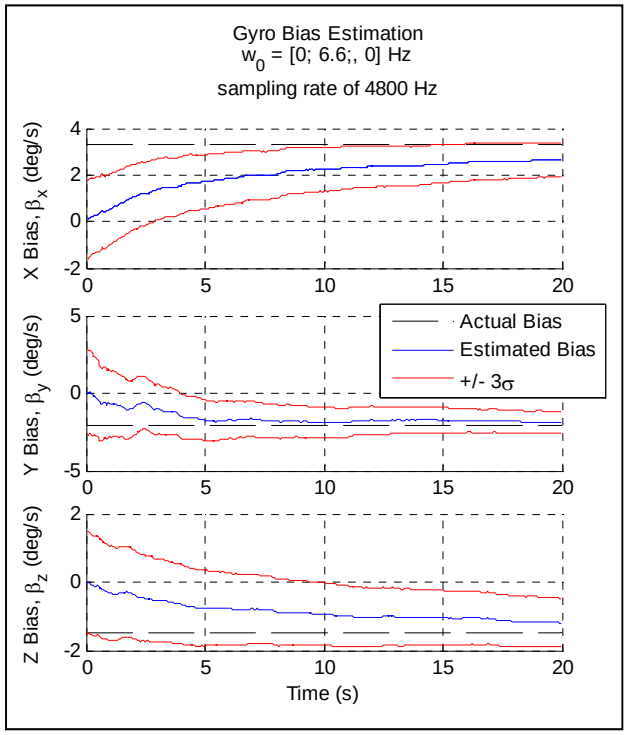


**Figure 42: EKF Bias Estimation of Simulated Data**

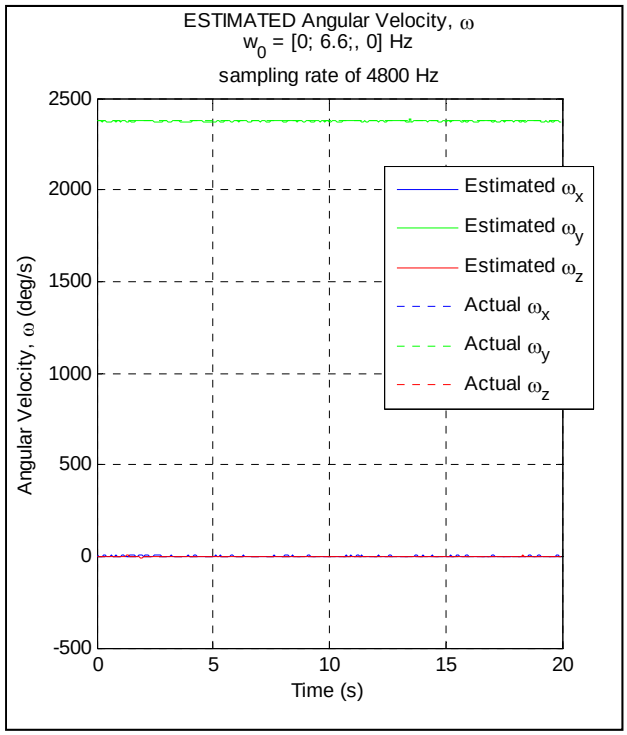


**Figure 43: EKF Estimated Angular Velocity of Simulated Data**

# ORGANIZATION

The project was funded by the National Science Foundation (NSF) and there were many individuals and organizations involved. The management structure is illustrated in Figure 44.

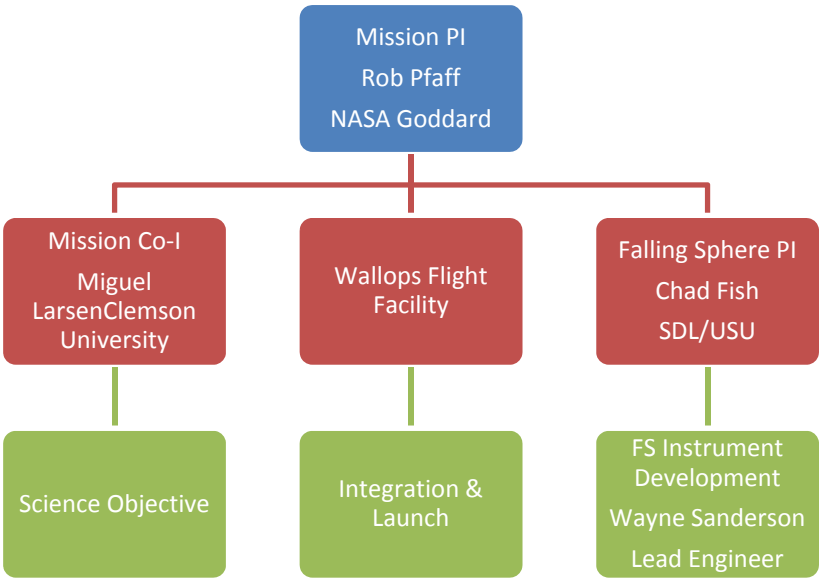


**Figure 44: High Level Organizational Chart**

For some of the specific responsibilities of SDL see Figure 45.

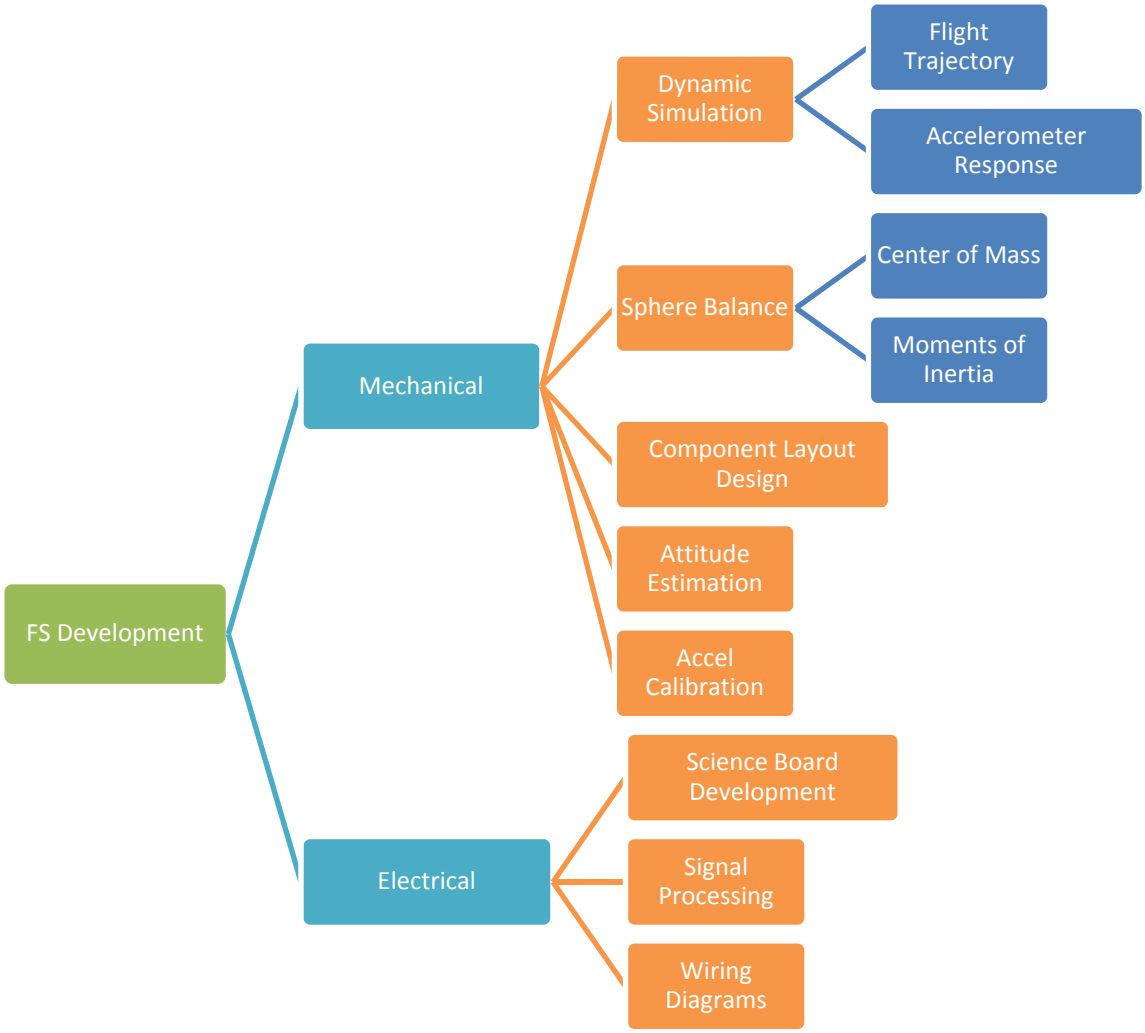


**Figure 45: SDL Work Breakdown**

For the individual roles and responsibilities of the author see Table 6.

**Table 6: Individual Roles & Responsibilities of Author**

| Category | Sub-category | Role & Responsibilities |
|---|---|---|
| Dynamic Simulation | Flight Trajectory | Finalized flight dynamics, including adding the effects of Mach flight, adding various types of drag on the sphere (pressure, skin friction, shockwave and drag due to excrescencies), and adding an atmospheric model for altitudes up to 1,000 km.<br>Verified rigid body dynamic equations of motion. |
| | Accelerometer Response | Added various sources of errors to the accelerometer signals to simulate real life instruments (scale factor, bias, noise, sensitivity, etc…). |
| Sphere Balance | Center of Mass | [*]Involved in the concept and design of the weight system to balance the sphere.<br>Refined technique and process of the multiple point weighing method used in SDL's NOVA lab.<br>Performed Balancing technique described in section § BALANCING.A: Center of Mass (CM) |
| | Moments of Inertia | [*]Designed component (blue nylon ring) key in stabilizing the sphere as a major axis spinner, or *oblate* spinner.<br>[*]Key individual in concept of performing the MOI measuring technique discussed in section § BALANCING.B: Moments of Inertia (MOI)<br>[*]Performed the MOI measurement technique.<br>Calculated nutation angle and precession rate from the inertia tensor. |
| Component Layout Design | None | Designed the layout of each component that goes into the sphere. There are physical constraints to each component as well as an effect on the MOI of the sphere. |
| Attitude Estimation | None | Developed the Kalman filter and smoother that estimates the orientation of the sphere throughout flight (based on ref [8]). |
| Accelerometer Calibration | None | Developed and wrote procedure for a vibe shake for the science accelerometer calibration.<br>[*]Designed sphere to vibe table interface fixture. |

[*]Assisted in task by Phillip Anderson, Grad Student Utah State University

# CONCLUSIONS

The desire of accurately modeling and understanding the atmospheric winds at a lower cost than current methods created the need for this particular project. The intent is to find a cheaper more robust way of measuring the winds in the Ionosphere than the chemical release method. This project, although not a complete success, shows that this objective can be accomplished. The sensors and equipment used are mostly commercial, off the shelf products. Even though the electronics were saturated due to undesired conditions, the rigid sphere can be a robust system, not needing the clear sky conditions or near dusk timing that is required by the chemical method. With a little better understanding of the electronics involved to improve the sphere, this method can be a superb one. For the current design, the flight spin rate must be 1.54 Hz or less to maintain a non-saturated state with the science accelerometers.

## A. Lessons Learned

There were many lessons learned and many more yet to be learned. There are many lessons that are naturally learned in a project like this. They are the things like how to manage a schedule, keeping on track with that schedule. Other things include how to better setup and conduct tests, and record processes and procedures, as well as communication between involved parties. However, there are a few lessons learned that are unique to this project.

a) The flight was intended to be in a certain environment, with expected conditions (i.e. spin rate). However, those conditions did not exist and the environment was a rather radical one that far exceeded the initial expectations. The capability of the sphere must be adjusted to compensate for more extreme conditions and/or environment. From this, however, came the better understanding of how the FS sensors responded to this extreme environment and some characterization was made, i.e. time constants, giving response time.

b) The deployment mechanism needed to be better understood. The Wallops Flight Facility was over the design, fabrication and integration of the deployment system of the sphere ejecting from the rocket. There were no set requirements on the deployment mechanisms other than ejection velocity. In order to facilitate a successful launch, hard test numbers should have been required.

c) A setup to analyze the post flight data needed to be in place before the actual flight. There were 3 out of 4 flight data samples lost during flight from the recording. The cause and the solution still remain unknown. Had all the tools and/or programs needed for looking at the recorded data been in place throughout all the calibration and characterization tests, this problem may have been detected before flight.

d) Since several people and organizations were a part of this project, it is essential to leave a paper trail of work performed. It became extremely difficult to pick up on a task where someone had left off where there was little to no understanding as to what the previous individual did or the direction in which he or she was heading in with the work.

e) Lastly, the importance the center of mass and MOI have on the balance of the sphere. The ability to change the center of mass (which also affects the moments of inertia) without opening the sphere or exposing the final assembly of electrical components was essential. This capability was designed, refined, and tested at SDL. Through the balancing of the sphere and with the blue nylon ring at the equator of the hemispheres, the sphere was spin stabilized and was changed from a minor axis spinner to a major axis spinner.

## B. Future Work

Complete analysis of the data is beyond the scope of this project and text. Further work and analysis is required to better understand the results of the flight data. Key to estimating the attitude would be to adjust the Kalman filter to accommodate the small sampling rate. With a fast enough CPU, the propagation step size could be set to a small enough step size to capture the dynamics between measurements to propagate the state and state covariance. Also, the attitude estimation could be further improved by having 12 states in the Kalman filter to include the 6-DOF in addition to the attitude error and gyro bias. The filter could also be improved by including measurement data from the gyros, accelerometers, magnetometer and GPS. The integration of the GPS data and the Inertial measurement data into the filter for attitude estimation is discussed in more detail in Refs [18], and [19].

Further process and analysis could be performed to determine if any neutral wind measurements could be determined from the flight data. Calculating the neutral winds is simply done by running the math prediction model (§ DYNAMICS) backwards.

From the information collected on the flight data from the first sphere, improvements or design changes should be noted and implemented into second sphere 41.090. Possible changes could include, but are not limited to, having a more precise IMU device with a sampling rate of 4.8 kHz or higher, different gains and settings for the science board to accommodate higher signals, different science accelerometers with a larger range of operating conditions, and possibly a different configuration for the science accelerometers to mitigate the effects of the accelerations see from spinning.

# REFERENCES


[1] M. Larsen, "Mesospheric and lower thermospheric wind observations over Puerto Rico," *Geophysical Research Letters,* vol. 27, no. 4, pp. 445-448, 2000.

[2] D. Hysell, M. Larsen, C. Barjatya, T. Wheeler, T. Bullett, R. Sarango, J. Chau and D. Sponseller, "Rocket and radar investigation of background electrodynamics and bottom-type scattering layers at the onset of equatorial spread F," *Annales Geophysicae,* vol. 24, no. 5, pp. 1387-1400, 2006.

[3] M. Larsen, A. Liu, R. Bishop, C. Gardner and J. Hecht, "TOMEX: A comparison of lidar and sounding rocke chemical tracer wind measurements," *Geophysical Research Letters,* vol. 30, no. 7, p. 1375, 2003.

[4] C. Philbrick, J. Noonan, E. Fletcher, T. Hanrahan, J. Salah, D. Blood, R. Olsen and B. Kennedy, "Atmospheric Properties from Measurements at Kwajalein," in *AFGL-TR-78-0195*, 1978.

[5] C. Philbrick, J. McIsaac, D. Frykund and R. Buck, "Atmospheric Structure Measurements from Accelerometer Instrumented Falling Spheres. In Wuppertal Univ. Sounding Rocket Program Aeronomy Project: Energy Budget Campaign 1980," 1981.

[6] C. Phillbrick, "Proc. 18th ESA Symposium European Rocket and Balloon Programmer and Related Research," Visby, Sweden, 2007.

[7] W. F. Philips, Mechanics of Flight, 2 ed., Hoboken, New Jersey: John Wiley & Sons, 2004.

[8] J. L. Crassidis and J. L. Junkins, Optimal Estimation of Dynamic Systems, New York: Chapman and Hall/CRC, 2004.

[9] S. A. Whitmore, "Supersonic Wings with Skin Friction: A Primer on Boundary Layers and SKin Friction," Logan, 2010.

[10] H. D. Curtis, Orbital Mechanics for Engineering Students, 2 ed., New York: Elsevier Ltd., 2010.

[11] J. Champion, "Building & Design Tips," 2009. [Online]. Available: http://www.jmrconline.org/buildinganddesign.htm.

[12] Y. A. Cengel and J. M. Cimbala, Fluid Mechanics Fundamentals and Applications, New York: McGraw-Hill, 2006.

[13] D. Schlegel, M. Folea, A. Roman and P. Nardin, "Surface Analysis of Machined Fiber Flass Composite Material," in *Recent Researches in Manufacturing Engineering*, N. B. Lupulescu, S. Yordanova and V. Mladenov, Eds., Brasov, WSEAS Press, 2011, pp. 152-155.

[14] M. J. Sidi, Spacecraft Dynamics & Control, Cambridge: Cambridge University Press, 1997.

[15] R. Boynton and K. Wiener, "Mass Properties Measurement Handbook," in *Annual Conference of the Society of Allied Weight Engineers*, Wichita, 1998.

[16] R. Boynton, "Mass Properties Measurement Errors Which Could Have Been Easily Avoided," in *58th Annual Conference of hte Soceity of Allied Weight Engineers*, San Jose, 1999.

[17] K. Wiener and R. Boynton, "Using the "Moment of Inertia Method" to Determine Product of Inertia," in *51st Annual Conference of the Society of Allied Weight Engineers*, Hartford, 1992.

[18] J. Farrell and M. Barth, The Global Positiong System & Inertial Navigation, New York: McGraw-Hill, 1998.

[19] M. Grewal, L. Weill and A. Andrews, Global Positioning Systems, Inertial Navigation, and Integration, New York: John Wiley & Sons, 2001.

[20] G. P. Sutton, Rocket Propulsion Elements, 7 ed., New York: John Wiley & Sons , 2001.

# APPENDIX

## A. Flight Environment

The predicted stagnation temperature and pressure of the sphere as well as predicted ambient temperature and pressure where calculated and compared to published results. Since the sphere had no pitot tube to measure the stagnation pressure, nor did it have any thermal sensors on the outer shell, there are no results to compare to. The predicted values are shown below in Figure 46 and Figure 47.

Although the calculated results indicate that the sphere would see temperatures higher than the material's melting point, with the sphere nutating as it was and given the short flight duration, the sphere did not see any adverse effects. This is verified in collecting data until very low altitudes (approximately 30 km or lower), indicating that the system was completely functional until then.

The ambient pressures and temperatures agree with the data presented in ref [20]. These results give an indication that the stagnation temperatures and pressures are at least on the right track as far as having the correct inputs to the calculations. These ambient conditions are shown in Figure 48 and Figure 49.

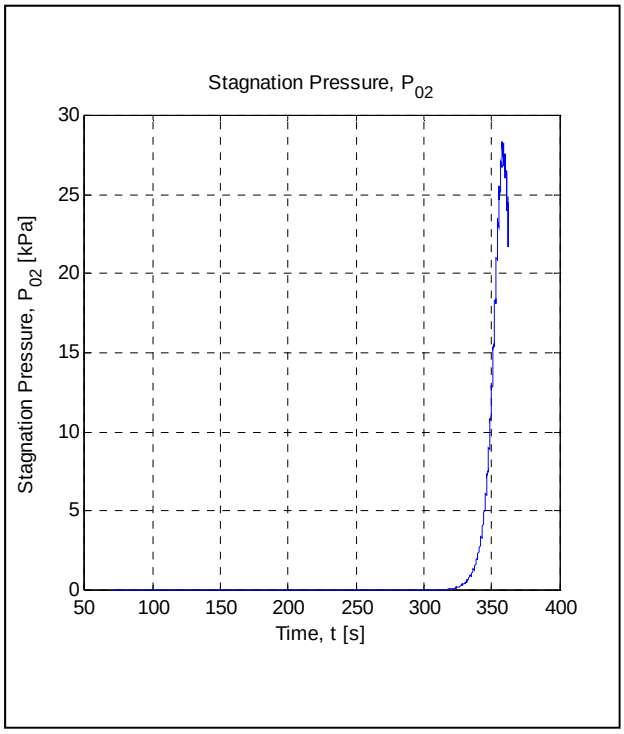


**Figure 46: Predicted Stagnation Pressure on the Sphere [kPa]**

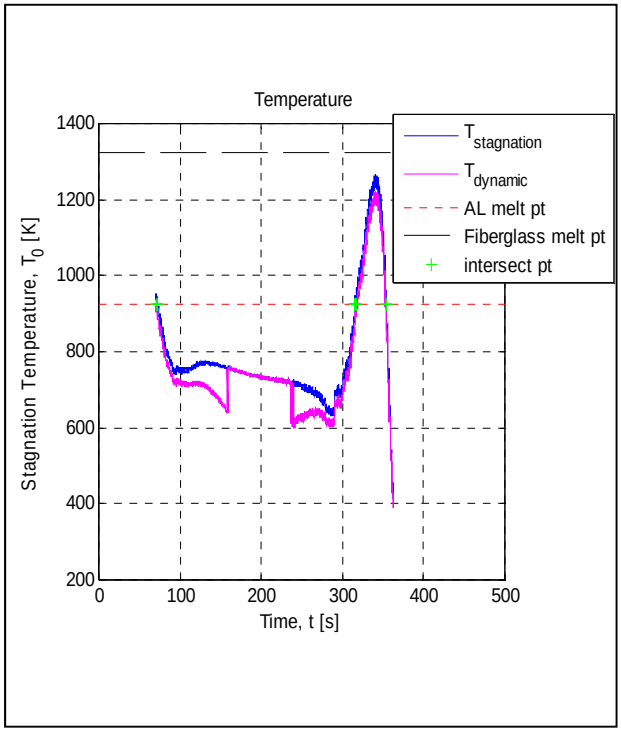


**Figure 47: Predicted Stagnation Temperature on the Sphere [K]**

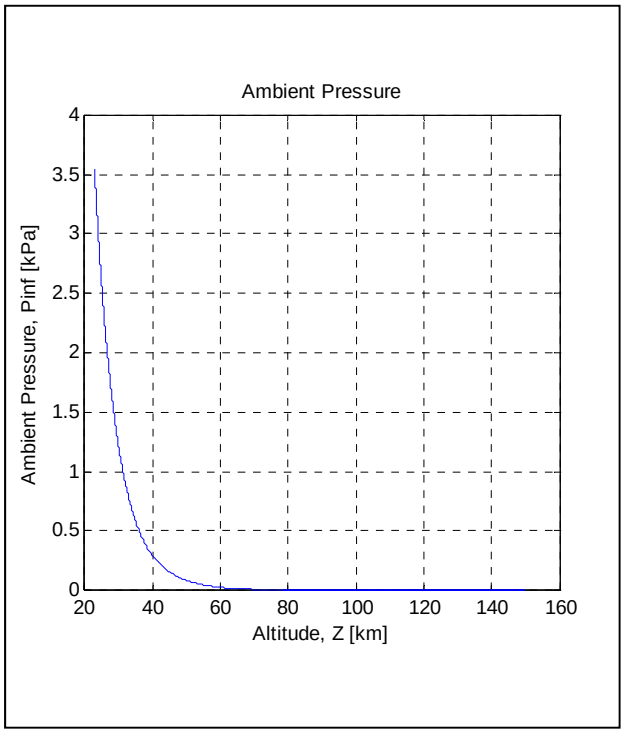


**Figure 48: Predicted Ambient Pressure as a function of altitude**

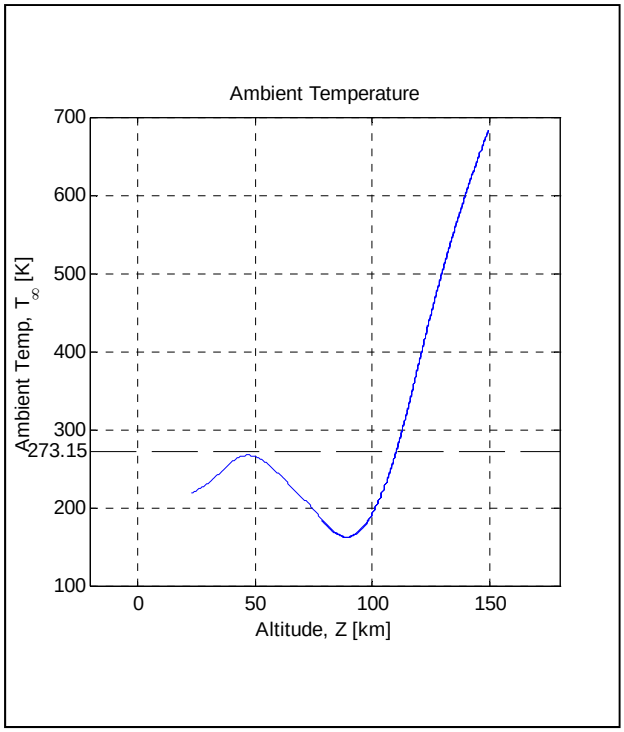


**Figure 49: Predicted Ambient Temperature as a function of altitude**

**B. Spec Sheets**

Instrumentation specifications

Science Accelerometers, by Wilcoxon Research:

# Model 731-207: Ultra low frequency seismic accelerometer

## Dynamic

Sensitivity, ±10%, 25°C.....10 V/g
Acceleration range.....0.5 g peak
Amplitude nonlinearity.....1%
Frequency response, nominal:
- ±5%.....0.6 - 650 Hz
- ±10%.....0.5 - 850 Hz
- ±3 dB.....0.2 - 1,300 Hz

Resonance frequency, mounted, nominal.....2.4 kHz
Transverse sensitivity, max.....1% of axial
Temperature response:
- –0°C.....–18%
- +80°C.....+8%

## Electrical

Power requirement: voltage source.....18 - 30 VDC
current regulating diode.....2 - 10 mA
Electrical noise, equiv. g, nominal:
- Broadband 2.5 Hz to 25 kHz.....2 µg
- Spectral 2 Hz.....0.28 µg/√Hz
- 10 Hz.....0.09 µg/√Hz
- 100 Hz.....0.03 µg/√Hz

Output impedance, max.....500 Ω
Bias output voltage, nominal.....10 VDC
Grounding.....case grounded

## Environmental

Temperature range.....0 to 80°C
Vibration limit.....50 g peak
Shock limit.....250 g peak
Electromagnetic sensitivity @ 60 Hz.....20 µg/gauss
Base strain sensitivity.....0.0005 g/µstrain
sealing.....hermetic design

## Physical

Weight.....50 grams
Case material.....316L stainless steel
Mounting.....10-32 UNF
Output connector.....10-32 coaxial

98069 Rev.C.2 1/01

(Courtesy Wicoxon Research Inc. and MEGGITT, www.meggitt.com)

µIMU sensors:

| PARAMETER | SPECIFICATION | | | | UNITS | CONDITIONS |
|---|---|---|---|---|---|---|
| **Operational Requirements** | | | | | | |
| Operating Supply Voltage | 8.0 to 13.0 | | | | VDC | Unregulated; Note 1 |
| Supply Current | 180 | | | | mA | typical |
| Alignment Error | ±1 | | | | % | |
| Mass | 95 | | | | grams | |
| **Acceleration** | **IM02** | **IM05** | **IM10** | | | |
| Dynamic Range | ± 2 | ± 5 | ± 10 | | g | |
| Offset | ±30 | ± 30 | ± 30 | | mg | 0 to 70 °C Maximum |
| Nonlinearity | ± 0.4 (± 1.0 ) | ± 0.4 (± 1.0 ) | ± 0.4 (± 1.0 ) | | % of FS | Typical (Maximum) |
| Noise | 0.6 (0.8) | 1.1 (1.3) | 2.1 (2.8) | | mg | Typical (Maximum), 1 σ |
| Digital Sensitivity | $9.1553 \times 10^{-5}$ | $2.2888 \times 10^{-4}$ | $4.5776 \times 10^{-4}$ | | g/bit | See Equation 1 on page 8 |
| Bandwidth [1] | 50 | 50 | 50 | | Hz | -3dB point; Note 2 |
| **Angular Rate** | **-0150C050** | **-0300C050** | **-0600C050** | **-1200C050** | | |
| Dynamic Range | ± 150 | ± 300 | ± 600 | ± 1200 | °/s | |
| Offset | +/-1.5 | +/-1.5 | +/-1.5 | +/-1.5 | °/s | 0 to 70 °C Maximum |
| Cross-Axis Sensitivity | +/-1 | +/-1 | +/-1 | +/-1 | % | Maximum |
| Nonlinearity | 0.1 | 0.1 | 0.1 | 0.1 | % of FS | Best fit straight line |
| Noise | 0.36 (0.95) | 0.56 (0.95) | 0.56 (0.95) | 0.56 (0.95) | °/s | Typical (Maximum), 1 σ |
| Digital Sensitivity | $6.8664 \times 10^{-3}$ | $1.3733 \times 10^{-2}$ | $2.7465 \times 10^{-2}$ | $5.4932 \times 10^{-2}$ | °/s/bit | See Equation 1 on page 8 |
| Bandwidth [1] | 50 | 50 | 50 | 50 | Hz | -3dB point; Note 2 |
| **Magnetic Field** | | | | | | |
| Dynamic Range | ±1.9 | | | | gauss | |
| Drift | 2700 | | | | ppm/°C | |
| Nonlinearity | 0.5 | | | | % of FS | Best fit straight line |
| Noise | 0.00056 (0.0015) | | | | gauss | Typical (Maximum), 1 σ |
| Digital Sensitivity | $8.6975 \times 10^{-5}$ | | | | gauss/bit | See Equation 1 on page 8 |
| Bandwidth [1] | 50 | | | | Hz | -3dB point; Note 2 |
| **Optional Acceleration** | **T35** | **T50** | | | | |
| Dynamic Range | ± 35 | ± 50 | | | g | |
| Digital Sensitivity | $1.6022 \times 10^{-3}$ | $2.2888 \times 10^{-3}$ | | | g/bit | See Equation 1 on page 8 |
| Noise | 1.0 | 1.0 | | | $mg/Hz^{½}$ | |
| Bandwidth [1] | 50 | 50 | | | Hz | -3dB point; Note 2 |
| **Temperature** | | | | | | |
| Digital Sensitivity | $1.8165 \times 10^{-2}$ | | | | °C/bit | |
| **Absolute Max Ratings** | | | | | | |
| Acceleration Powered | 2000 max | | | | *g* | Any axis 0.5ms |
| Input Voltage Range | -0.3 (min) +13 (max) | | | | VDC | Note 1 |
| Operating Temperature | **C - Commercial** | **M - Military** | | | °C | |
| Temperature Range | 0 to +70 | -40 to +85 | | | | |
| Storage Temperature | -25 to +85 | | | | °C | |

Typical Values at 25°C, $V_{supply}$ = 8.3 VDC, 0 °/s, unless otherwise noted.
**Note: µIMU configurations are not subject to ITAR export controls.**

1. When using a USB Data Acquisition Board specified for a maximum voltage of 8.5 volts applying a higher voltage will damage the USB Data Acquisition Board. Optional 12 V version of USB DAQ is available.
2. Other bandwidth configurations are available upon request.